https://doi.org/10.5194/essd-2026-711
Preprint. Discussion started: 2 November 2026
© Author(s) 2026. CC BY 4.0 License.



Open Access Earth System Science Data Discussions

MioTEX: A comprehensive GDGT-based ocean temperature compilation for the Miocene

Alexandra Auderset[1*], Xiaoqing Liu[2*], Neeraj S. Shah[3], Sarah J. Feakins[4], Francesca Sangiorgi[5], Amelia Shevenell[6], Kasia K. Śliwińska[7], Appy Sluijs[5], Evi Wubben[5], Yi Ge Zhang[8], Sevasti Modestou[9], Sindia M. Sosdian[10] and Ann Holbourn[11†]

[1] School of Ocean and Earth Science, University of Southampton, Southampton, SO14 3ZH, UK
[2] Department of Earth, Atmospheric, and Planetary Sciences, Purdue University, West Lafayette, IN 47907, USA
[3] Independent researcher
[4] Department of Earth Sciences, University of Southern California, Los Angeles, CA 90089, USA
[5] Department of Earth Sciences, Faculty of Geosciences, Utrecht University, Utrecht, 3584 CB, the Netherlands
[6] College of Marine Science, University of South Florida, St. Petersburg, FL 33701, USA
[7] Department of Geo-energy and Storage, Geological Survey of Denmark and Greenland (GEUS), Copenhagen, 1350 Copenhagen K, Denmark
[8] State Key Laboratory of Deep Earth Processes and Resources (DEEPER), Guangzhou Institute of Geochemistry, Chinese Academy of Sciences, Guangzhou, 510640, China
[9] Department of Geography and Earth Sciences, Northumbria University, Newcastle upon Tyne, NE1 8ST, UK
[10] School of Earth and Environmental Sciences, Cardiff University, Cardiff, CF10 3AT, UK
[11] Institute for Geosciences, Kiel University, Kiel, 24118, Germany

[*] These authors contributed equally.
[†] Deceased.

Correspondence to: Alexandra Auderset (a.auderset@soton.ac.uk), Xiaoqing Liu (xiaoqingliu@purdue.edu)

Abstract. The Miocene epoch (~23 to 5.3 million years ago) was a period when global mean temperatures were warmer than today, with estimated atmospheric CO_2 levels similar to those expected in coming centuries. Climate models generally underestimate reconstructed Miocene global mean and high-latitude ocean temperatures, a persistent discrepancy that raises questions about both the reliability of proxy reconstructions and the ability of climate models to represent warm climate states. Resolving this discrepancy requires a critical, unified reevaluation of the existing proxy record. Here we compile and reevaluate existing ocean temperature records reconstructed using the TEX_{86} paleothermometer. The TEX_{86} paleothermometer, which derives upper ocean temperatures from the distribution of the membrane lipids of marine archaea, has been widely used to reconstruct past sea surface and shallow subsurface (0-200m) temperatures. Here, we introduce MioTEX, a global compilation of Miocene ocean temperature records based on the TEX_{86} proxy. This effort, developed within the MioOcean initiative, applies uniform screening criteria and calibration methods to published records from 46 sites spanning multiple ocean basins. We find distinct temperature variations among different latitudinal bands and ocean basins, as well as absolute temperature differences arising from the choice of calibration. Compared with previous SST reconstructions suggesting an Early to Middle Miocene collapse and Late Miocene establishment of the modern meridional SST gradient, our standardised, multi-site synthesis quantifies when and where such gradient changes occurred across ocean basins, with the strongest cooling recorded

https://doi.org/10.5194/essd-2026-711
Preprint. Discussion started: 2 November 2026
© Author(s) 2026. CC BY 4.0 License.



Open Access Earth System Science Data Discussions

at high-latitude sites in the South Atlantic and Southwest Pacific. The MioTEX dataset is publicly available at Zenodo (https://doi.org/10.5281/zenodo.22258386, Sosdian et al., 2026) and presented on an interactive Streamlit-based web platform, allowing users to explore data, apply different calibrations, and test screening criteria.

Short summary. Climate models struggle to reproduce Miocene (23–5.3 million years ago) ocean temperatures, a period when CO_2 levels overlapped near-future projections. Understanding this model–data mismatch requires evaluating available temperature records and uncertainties. We compiled MioTEX, a standardized global dataset of Miocene ocean temperatures from 46 sites using the TEX_{86} proxy. Calibration choices influence absolute temperatures. MioTEX is freely accessible via an interactive web platform.

1 Introduction

The Miocene epoch (23.03–5.33 million years ago, Ma) is a time interval of generally warm climates, with a global mean surface temperature estimated to be 5-11°C warmer than the preindustrial era (Flower and Kennett, 1994; Cramer et al., 2011; Burls et al., 2021) and with continental positions similar to the present except for a few key differences (Lagabrielle et al., 2009; O'dea et al., 2016; Steinthorsdottir et al., 2021). Miocene climate evolution is of interest both for understanding past and future climate evolution. In the Early to Middle Miocene (~23.0-13.8 Ma), the Antarctic ice sheet experienced large-scale advances and retreats (Flower and Kennett, 1994; Shevenell et al., 2008; Gasson et al., 2016; Liebrand et al., 2017) but the Northern Hemisphere lacked major ice sheets. In the late Early to Middle Miocene, the Earth went through a ~2.5 million-year period of warmth known as the Miocene Climate Optimum (MCO; ~16.9 to 14.7 Ma), where average surface temperatures were 7-8°C higher than modern, with pronounced polar amplification (Steinthorsdottir et al., 2021). Significant Antarctic ice sheet expansion and global cooling occurred during the Middle Miocene Climatic Transition (MMCT; ~14 Ma) (Shevenell et al., 2008; Miller et al., 2020). In the Late Miocene (~7-5.4 Ma), there was sustained global cooling and the establishment of modern meridional thermal gradients (Herbert et al., 2016; Zhang et al., 2014), which was accompanied by global changes in terrestrial vegetation (Pound et al., 2012). Sedimentary archives of a warmer-than-modern and dynamic climate of the Miocene provide an opportunity to gain insight into processes influencing and influenced by climatic warming, thus helping us predict the potential patterns and impacts of future warming (Steinthorsdottir et al., 2021).

Synthesizing existing data on Miocene climate, including temperatures, precipitation, atmospheric CO_2 concentrations, advances our understanding of climate feedbacks and interactions, with implications for ongoing climate change. The MioOcean effort (Sosdian et al., this volume) compiles proxy records used to reconstruct sea surface temperatures (SST) from marine sediment archives. These proxies/paleothermometers include Mg/Ca ratios of planktic foraminiferal tests, the alkenone unsaturation index ($U^{K}_{37'}$), carbonate clumped isotopes (Δ47), and the TetraEther indeX of tetraethers consisting of 86 carbon atoms (TEX_{86}) based on the distribution of archaeal membrane lipids preserved in sediments. This proxy is based on the relative abundance of cyclopentyl moieties among isoprenoid glycerol dibiphytanyl glycerol tetraethers (GDGT) lipids, which

https://doi.org/10.5194/essd-2026-711
Preprint. Discussion started: 2 November 2026
© Author(s) 2026. CC BY 4.0 License.



are produced by marine nitrifying archaea of the order Nitrososphaerales and preserved in marine sediments (Elling, Inglis et al., 2026). In this study, we synthesize Miocene global surface and subsurface ocean temperature records derived exclusively from TEX_{86}. GDGTs are primarily produced in the water column near the nutricline, usually at depths between approximately 50 and 250 meters (e.g., Sinninghe Damsté et al. (2002)). The depth from which sedimentary GDGTs originate is debated ((Schouten et al., 2002; Taylor et al., 2013; Tierney and Tingley, 2014; Ho and Laepple, 2016; Hurley et al., 2018; Rattanasriampaipong et al., 2022; Van Der Weijst et al., 2022; Zhang and Liu, 2018), leading to a range of GDGT-based indices and calibrations for converting TEX_{86} to temperature and different interpretations of the depth represented by the TEX_{86} signal. Several studies calibrate TEX_{86} to SST or temperatures within the mixed layer, as well as to integrated temperatures from 0-200 meters depth (Kim et al., 2008; Kim et al., 2010; Tierney and Tingley, 2014). The global core-top TEX_{86} tracks the surface-shallow-subsurface (<200 m) latitudinal gradient (Zhang and Liu, 2018). However, the nutricline depth varies from location to location and some studies suggest a deeper upper limit, proposing depths of 100-350 meters (Van Der Weijst et al., 2022) or 100-250 meters (Fokkema et al., 2024) as potential endmember possibilities, depending on local ecological and oceanographical evidence.

Here we compile Miocene TEX_{86} data from multiple ocean basins using a consistent method that applies calibrations following the most recent proxy insights and the same screening criteria to all records. We subsequently systematically investigate the ocean temperature evolution across different regions during the Miocene. The compiled dataset will be valuable for the overall MioOcean effort, allowing for an in-depth multi-proxy comparison and the Miocene Modelling Intercomparison Project (MioMIP) to evaluate absolute temperatures and to evaluate models' performance in simulating Miocene ocean temperature patterns. We present the compiled data through a web application built with Streamlit, an open-source Python-based framework. This application allows users to explore and visualize the data by switching among available TEX_{86}-temperature calibrations, selecting different latitudinal bands, and applying various screening criteria, among other features.

2 Data and methods

2.1 Data description and availability

The MioTEX compilation is released as part of the MioOcean database; a full description of the database structure, file formats, column definitions, units, and quality flags is provided in the companion MioOcean database paper (Sosdian et al., this volume). In brief, the TEX_{86} records are distributed as a proxy-specific file (tex86_product.xlsx) containing the raw and standardised GDGT/ TEX_{86} measurements along with the full suite of calibration outputs and associated metadata. Each file is organised into three worksheets: a Data sheet with all sample-level measurements and calculated temperatures; a Columns sheet defining every column name, data type, and unit; and a Metadata sheet documenting provenance (compilation date, input-file hash, and Git commit). Both the published and MioOcean-recommended ages are reported ("Published age (Ma)" and "MioOcean recommended age (Ma)"). For the analyses and figures in this study, we chose the "MioOcean recommended age (Ma)" (see Drury et al., this volume). The same records are also integrated into the reduced multi-proxy compilation

https://doi.org/10.5194/essd-2026-711
Preprint. Discussion started: 2 November 2026
© Author(s) 2026. CC BY 4.0 License.



(mio_ocean_product.xlsx), which retains a single recommended (or Monte Carlo–ensemble) calibration per proxy for cross-proxy and model–data comparison. The dataset is version-controlled on GitHub (https://github.com/audersea/mio_compilation), archived on Zenodo (https://doi.org/10.5281/zenodo.22258386, Sosdian et al. 2026) and on the MioOcean website (https://www.mioocean.com/download-data/), and can be explored interactively via the MioTEX (https://www.mio-tex.streamlit.app/) and MioOcean (https://www.mio-ocean.streamlit.app/) Streamlit dashboards or directly via the MioOcean website: https://www.mioocean.com/temperature-proxies/tex86/ or https://www.mioocean.com/explore-data/.

2.2 Data collection

TEX_{86}-based upper ocean temperature data were compiled from published papers and public data portals (e.g., Pangaea, NOAA, or Zenodo). Our starting point for the data compilation was TEX_{86}-based entries from the Bolin Centre Miocene temperature portal (https://bolin.su.se/data/miocene-temperature-portal). When publications included data extending beyond the Miocene, we incorporated the full published dataset, although only the Miocene interval was used for interpretation. In cases where raw data were unavailable online, they were requested from the corresponding authors. An overview of the compiled 46 sites and other collected information can be found in Table A1 and Supplementary Material.

2.3 Paleo-coordinates reconstructions

Following the MioMIP2 Phase 2 experimental design (Burls et al., 2026), paleo-coordinates for the sites included in this compilation were calculated by rotating modern site locations to their positions at the age recommended by MioOcean synthesis using the GPlately Python library (Mather et al., 2023) and the plate tectonic reconstruction of (Zahirovic et al., 2022), employing the paleomagnetic reference frame of (Merdith et al., 2021) and using the African plate (plate ID 701701) as the anchor plate.

2.4 (Re)calculated indices

All compiled TEX_{86} data were screened for non-thermal effects before being consistently converted to temperature to minimize the effect of confounding factors on GDGT distributions, including the influence of methanotrophic and methanogenic archaea, deep-water produced GDGTs (Taylor et al., 2013), and soil-derived GDGTs (Weijers et al., 2006). The criteria used to screen TEX_{86} data and their associated cutoff ranges, based on the original publications, are listed in Table A2. These criteria include the Branched versus Isoprenoid Tetraether (BIT) index (Hopmans et al., 2004), methane index (MI) (Zhang et al., 2011), GDGT-2/crenarchaeol ratios (Weijers et al., 2011), GDGT-0/crenarchaeol ratios (Blaga et al., 2009), %GDGT-0 (Sinninghe Damsté et al., 2012), GDGT-2/GDGT-3 ratios (Taylor et al., 2013), and ΔRing Index (Zhang et al., 2016). As these confounding factors may influence the validity of TEX_{86}-derived paleotemperatures, reevaluating previously published TEX_{86}-derived temperature data using these criteria is appropriate. Unfortunately, some earlier publications did not report fractional abundances for all GDGTs, which prevents assessment of potential non-thermal factors.

https://doi.org/10.5194/essd-2026-711
Preprint. Discussion started: 2 November 2026
© Author(s) 2026. CC BY 4.0 License.



Open Access Earth System Science Data Discussions

2.5 Temperature calibrations and uncertainties

Over the years, several sea surface, as well as subsurface, temperature calibrations were proposed (Table A3) for the GDGT-derived TEX_{86} temperature reconstructions. There is no single calibration that is suitable for all geographic settings and all geological time intervals, as noted in the review and synthesis by Bijl, Śliwińska et al. (2025). Therefore, we do not recommend applying a single TEX_{86}-calibration across globally distributed sites. This includes not favoring either the SST or SubT calibration, because the dominant export depth remains difficult to constrain (Bijl, Śliwińska et al., 2025, Elling, Inglis et al., 2026), despite the evidence that GDGT production occurs primarily in subsurface waters. For MioOcean, we will report all calibrations in the proxy-specific output, but for the overall MioOcean temperature product, we will use a latitude-specific Monte Carlo approach that combines several sea surface temperature calibrations to capture the full range of calibration uncertainty. We highlight and quantify potential absolute temperature discrepancies based on the calibration of choice in Sect. 3.2.

2.5.1 Sea surface temperatures

As noted in Sect. 2.5, no single TEX_{86} calibration is universally appropriate for all Miocene sites and geographic settings. Within this compilation, we therefore apply a range of the most widely used SST calibrations to allow users to assess calibration-dependent differences. These include the global core top calibration of Kim et al. (2008) (Kim08), TEX_{86}^{H} and the TEX_{86}-linear calibration of Kim et al. (2010) (Kim10H and Kim10linear, respectively); and a Bayesian, spatially-varying regression model (with a prior standard deviation of 6 and 1000 draws) by Tierney and Tingley (2014) (BAYSPAR-SST). We additionally apply the SST calibration from O'Brien et al. (2017) (O'Brien17), a TEX_{86}-linear calibration, and Liu et al. (2009) (Liu09), a TEX_{86}-reciprocal calibration, both developed for past greenhouse climates (Cretaceous and Eocene, respectively), as well as the machine-learning-based OPTiMAL calibration (Dunkley Jones et al., 2020; DJ20), TEX_{86}^{L} (Kim et al., 2010; Kim10L) suitable for low-temperature regions, and the recent calibration of Varma et al. (2024) applying the "complete dataset" excluding OH-GDGTs (Varma24). All calibration outputs are retained in the proxy-specific compilation file for users requiring detailed, calibration-level information. Published SST values from original publications are also reported for comparison.

For the MioOcean multi-proxy temperature compilation (Sosdian et al., this volume), TEX_{86}-derived upper ocean temperatures (UOT) were calculated using a Monte Carlo ensemble approach (N = 10,000 draws) with latitude-dependent calibration weighting. At low to mid latitudes (−40°S to 50°N), only TEX_{86}^{H} (Kim et al., 2010; σ = RSE = ±2.5°C) and BAYSPAR SST (Tierney and Tingley (2014); $\sigma = (p84 - p16) / 2$) are applied, with equal weights. At mid to high latitudes (≥50°N or ≤−40°S), only BAYSPAR SST and OPTiMAL (Dunkley Jones et al. (2020); σ = OPTiMAL standard deviation) are used, with equal weights. The latitude regime is fixed per site from its mean paleolatitude across the full record. When a calibration is unavailable for an individual sample, it is excluded and the remaining calibration is assigned full weight. Ensemble percentiles

https://doi.org/10.5194/essd-2026-711
Preprint. Discussion started: 2 November 2026
© Author(s) 2026. CC BY 4.0 License.



are calculated by collapsing across calibrations and Monte Carlo draws simultaneously, with the 2.5th, 16th, 50th, 84th, and 97.5th percentiles reported for each sample.

We adopt the compromise approach embedded within UOT as the primary MioOcean temperature because it is directly comparable to the surface- and mixed-layer-referenced proxies used elsewhere in the compilation (e.g., Mg/Ca, $\delta^{18}O$, $U^{K}_{37'}$, Δ47). SubT is retained to interrogate the vertical structure of the temperature signal, as described above.

2.5.2 Subsurface temperatures

Because the dominant export depth of GDGTs remains difficult to constrain, subsurface temperature reconstructions (SubT) are reported alongside SST estimates for each site. We apply three depth-integrated calibrations representing different estimates of GDGT production depth: (1) 0–200 m, including the Kim12_0-200m calibration (Kim et al., 2012) and BAYSPAR-SubT (Tierney and Tingley (2014); a prior standard deviation = 6, 1000 draws), and (2) 100–250 m, including the HL16_100-250m calibration (Ho and Laepple, 2016). These depth ranges reflect the range of plausible GDGT production depths (Schouten et al., 2002; Taylor et al., 2013; Tierney and Tingley, 2014; Ho and Laepple, 2016; Hurley et al., 2018; Rattanasriampaipong et al., 2022; Van Der Weijst et al., 2022; Zhang and Liu, 2018). For the MioOcean multi-proxy compilation (Sosdian et al., this volume), subsurface temperatures were calculated using a Monte Carlo ensemble approach (N = 10,000 draws) with equal weighting among all three calibrations. Ensemble percentiles are reported at the 2.5th, 16th, 50th, 84th, and 97.5th levels, consistent with the UOT ensemble approach above.

2.5.3 Antarctic temperatures

The application of TEX_{86} to Antarctic coastal regions is subject to additional complexities. Therefore, this section discusses these issues and describes our approach to reconstructing TEX_{86}-based ocean temperatures at Miocene Antarctic sites. For temperature reconstructions proximal to the present-day glaciated Antarctic continent, several approaches and TEX_{86} calibrations have been used, but no consensus has been reached.

Over the Antarctic continental shelves, where most published Miocene records originate, GDGTs are currently produced during the austral spring at water depths between 0 and 50 meters (Church et al., 2003; Murray et al., 1998; Shevenell et al., 2011; Tolar et al., 2016). To build a regional relationship between TEX_{86} and SST, surface sediment TEX_{86} values, paired with measured average surface ocean temperatures (0-50 m) from the Western Antarctic Peninsula and East Antarctic continental shelves (Shevenell et al., 2011; Vadman, 2021; Browne et al., 2022), were added to the global calibration data set, with Arctic Ocean and non-surface (>2 cm below sea floor) sediment samples removed (Shevenell et al., 2011). Arctic Ocean samples were excluded because polar TEX_{86} values can exhibit distinct relationships with temperature compared with the global calibration, potentially reflecting regional differences in the temperature response of GDGT-producing archaea (Pearson and Ingalls, 2013). The resulting TEX_{86}-derived temperatures were within ~1°C of measured temperatures when using a regional linear calibration (Shevenell et al., 2011) or the Bayesian calibration of (Tierney and Tingley, 2014). This approach has resulted in modern to Holocene SST records that are consistent with both measured surface ocean temperatures and temperature trends

https://doi.org/10.5194/essd-2026-711
Preprint. Discussion started: 2 November 2026
© Author(s) 2026. CC BY 4.0 License.



and magnitudes of change similar to those observed in ice core records, providing additional confidence in the TEX_{86} proxy in Antarctic margin sediments (Shevenell et al., 2011; Mulvaney et al., 2012).

In the Antarctic Ross Sea region (AND-2A) and Wilkes Land (Site U1356) (e.g., Levy et al., 2016; Sangiorgi et al., 2018) were reconstructed using TEX^{L} (Kim et al. 2010, 2012). Although the resulting temperature estimates generally agree with those derived from other proxies (e.g., Warny et al., 2009; Sangiorgi et al., 2018), it is clear that TEX^{L} may not exclusively reflect temperature, as variations in the GDGT2 to GDGT3 ratios, which can be influenced by local environmental conditions (Taylor et al., 2013), strongly affect the TEX^{L} index. Recalibrated TEX_{86}-based T using the Kim et al. (2010) and BAYSPAR calibration for Site U1356 were later published in Hartman et al. (2018). More recently, Duncan et al. (2022) applied the machine learning-based temperature OPTiMAL (Optimised Palaeothermometry from Tetraethers via MAchine Learning) calibration (Dunkley Jones et al., 2020) for presenting temperature trends during the Oligocene to Quaternary period obtained in several sediment records from the Ross Sea.

The use of different calibrations demonstrates how challenging it is to reconstruct temperatures in polar (Antarctic) regions. Absolute cold-end temperatures at these sites carry additional analytical uncertainty associated with early-HPLC data (isomer detection near the detection limit, integration, and chromatography), and a dedicated re-evaluation of Antarctic-shelf TEX_{86} using re-integrated UHPLC datasets is crucial. Recently, a new temperature proxy, including isoprenoidal hydroxylated GDGTs (OH-isoGDGTs) (TEX_{86}^{OH}, Varma et al., 2024), has been explored and appears promising for providing reliable polar temperatures, as OH-isoGDGTs are highly abundant in polar regions. However, the environmental and ecological controls on OH-isoGDGT distributions remain incompletely understood, including the extent to which these compounds preferentially record colder temperatures and their uncertain depth of production (Bijl, Śliwińska et al., 2025). Moreover, temperature responses of GDGT-producing populations may vary among environments, reflecting adaptation to different thermal regimes and warranting caution when applying a single calibration across broad temperature ranges (Bijl, Śliwińska et al., 2025). To date, only one study has reported Miocene OH-isoGDGTs records (Wubben et al., 2026).

2.5.4 Temperature uncertainties

The uncertainties of TEX_{86}-based absolute temperatures come from both calibration error and analytical error. Since the analytical error is smaller, the uncertainties shown in our compilation reflect only the calibration error (Table A3) as reported by the original publications. These calibration errors are represented either as the residual standard error of a regression or as a statistical summary (5th, 50th, and 95th percentiles). For the Monte Carlo SST and SubT approaches, ensemble percentiles are reported at the 2.5th, 16th, 50th, 84th, and 97.5th levels.

2.6 Latitudinal and regional temperature stacks

Apart from (re)calculating GDGT indices (Sect. 2.2) and applying multiple temperature calibrations (Sect. 2.3), we categorized each core site according to its modern latitude into four bands: low latitude (0º-20ºN/S), middle latitude (20º-40ºN/S), northern mid to high latitudes (>40ºN), and southern mid to high latitudes (>40ºS). Because we use each site's modern coordinates

https://doi.org/10.5194/essd-2026-711
Preprint. Discussion started: 2 November 2026
© Author(s) 2026. CC BY 4.0 License.



rather than time-evolving paleopositions, each site retains the same latitudinal classification throughout its record. We deliberately adopt a fixed site classification because some records span more than 20 million years of plate motion and would otherwise move between latitude categories through time. Using evolving paleolatitudes would introduce artificial discontinuities in the latitudinal stacks, as individual sites could switch categories during their record and, in the MioOcean framework, potentially transition between calibration regimes. This would make reconstructed temperature trends sensitive not only to climate change but also to changes in site classification.

Within the northern mid to high latitudes, we distinguish a "transition North" subcategory (40º-50ºN) from the high-latitude sites proper (>50ºN). This distinction is particularly relevant for regions such as the North Atlantic, where the Gulf Stream–North Atlantic Current forms a sharp sea-surface temperature front with gradients of up to ~2ºC per 100 km, producing total cross-frontal temperature contrasts of up to ~10ºC across the current (Tsopouridis et al., 2021). Sites poleward of 50ºN and those between 40ºS and 60ºS are further divided by ocean basin into Atlantic and Pacific sectors (Atlantic assigned to longitudes 80ºW to 20ºE, Pacific otherwise), reflecting distinct water masses bathing each sector at a given latitude. Unlike the northern hemisphere, the southern hemisphere has no equivalent "transition" subcategory; sites progress directly from the 20º-40ºS middle-latitude band to the Atlantic/Pacific subdivision. Core sites surrounding Antarctica (>60ºS) are assigned to a separate "Antarctic" latitudinal subcategory, without further subdivisions by ocean basin, because they consistently record lower temperatures than sites in the southern high latitudes (Figs. 4 & 5). In addition to latitude, we record each site's ocean basin, region within the ocean basin, modern water depth, and whether each core site is on the shelf or in the open ocean (Table A1).

2.7 Interactive data visualisation

Data visualization is an important component for the analysis and interpretation of large data sets like the Miocene TEX_{86} compilation. To support this, we generated a Python-based Streamlit dashboard: https://www.mio-tex.streamlit.app/, which can also be directly accessed via the MioOcean website: https://www.mioocean.com/temperature-proxies/tex86/. The dashboard allows the users to explore Miocene TEX_{86}-derived SST data interactively through adjusting parameters and temperature calibrations, filtering data based on GDGT indices, regions, or latitudinal categories, and instantly viewing the results of these selections, thereby facilitating a deeper understanding of this complex dataset.

This interactive function is particularly valuable for researchers working with Miocene paleotemperature data, while also making the dataset more accessible to non-specialist users interested in past climate change.

The Streamlit dashboard is directly connected to the most recent uploaded data compilation files published on Zenodo (link to follow) and can be continuously updated and adjusted based on the user's needs. More information on the data management and storage can be found in the MioOcean paper (Sosdian et al., this volume).

https://doi.org/10.5194/essd-2026-711
Preprint. Discussion started: 2 November 2026
© Author(s) 2026. CC BY 4.0 License.



3 Results and data interpretation

The comprehensive compilation of all GDGT-based sea surface and subsurface temperature records from the literature and its careful reevaluation based on different calibrations and excluding criteria allows us to increase our knowledge about the temperature evolution in the Miocene and understand calibration differences and applications.

3.1 New Miocene data coverage

The new dataset consists of 46 core sites: 16 in the Atlantic, 14 in the Pacific, 6 in the Indian Ocean, and 10 in the Southern Ocean (Table A1 and Figure 1), comprising 21 Ocean Drilling Program (ODP), 9 International Ocean Drilling Program (IODP), and 7 Deep Sea Drilling Program (DSDP) sites, plus 9 additional non-ODP/IODP/DSDP sites: AND-2A, CIROS-1, and CRP-2 (Antarctic margin drill cores), McMurdo Erratics (glacial erratic clasts), Agios Myron, Govone, Potamida, and Vicchio Fm (Mediterranean/Tethys terrestrial outcrops), and QZ6 (onshore borehole in China). Within the Miocene interval, most data points come from the tropical oceans (n = 1,404), followed by the subtropics (n = 422). The modern water depths range from 50 to 4,742 meters, with modern sea surface temperatures spanning from -1 to 29°C.

All the reported core sites include at least some Miocene data points. We also include TEX_{86} data for time intervals expanding before the onset of the Miocene, or expanding into the younger epoch, when a publication reports data from other time intervals from the same site outside the Miocene. Data resolution varies from ~3 to ~2000 thousand years (kyr) per sample, with an average of ~250 kyr.

3.2 Screening for non-thermal influences

We applied screening thresholds for various indices (Table A2) to the TEX_{86} data. Individual criteria removed between ~3% and ~39% of the data points. The most significant reduction occurs with the [2]/[3] ratio (GDGT-2/GDGT-3), which excludes 2167 data points at a threshold of 5 (~39% of the entire dataset). Values above 5 indicate a substantial contribution from a deeper-dwelling archaeal clade rather than the shallow, surface-temperature-tracking population TEX_{86} is intended to record (Taylor et al., 2013). The next most restrictive criteria are the branched vs. isoprenoid index (BIT) at a threshold of 0.4, which excludes 1439 data points (~26% of the entire dataset; ~33% of the 4390 samples with a valid BIT measurement), and the ring index delta (Δ<−0.3 or >0.3; 1436 points, ~26%).

For sites near the continent and at water depths shallower than 400 m, where soil-derived isoGDGT input could influence TEX_{86}-derived temperatures, we recommend a combined screening using both BIT and #ringstetra (Sinninghe Damsté, 2016). Compared to the BIT screening alone, this combined approach removes only 66 samples out of 1594 samples with both indices measured (~1% of the entire dataset; Figure 2). However, because relatively few studies report brGDGTs, or at least the specific brGDGTs required for #ringstetra estimates, many samples lack the data needed for this combined screening. These samples were retained in the compilation, but potential terrestrial influence cannot be assessed using #ringstetra. Consequently, the number of data points affected by terrestrial influence may be higher than indicated by the combined screening.

https://doi.org/10.5194/essd-2026-711
Preprint. Discussion started: 2 November 2026
© Author(s) 2026. CC BY 4.0 License.



Applying the MI threshold (>0.5) removes ~3% of the data (171 points), %GDGT-0 (>67) removes ~8% (463 points), and %GDGTRS (>30) removes ~4% (209 points; Figure 2). The relatively low percentage of data excluded by MI likely reflects its widespread adoption in the TEX_{86} community as an indicator of non-thermal influences. GDGT-0/cren (>2) removes ~9% (505 points), and GDGT-2/cren (>0.2) removes ~17% (955 points), the fourth-largest single exclusion criterion, after [2]/[3], BIT, and ring index delta. Applied on its own, #ringstetra (>0.7) removes ~3% (149 points; ~9% of the 1623 samples with a valid #ringstetra measurement).

All combined, 3069 data points (~56% of the entire dataset) would be classified as "excluded" by at least one criterion. However, rather than removing these data points from the MioTEX compilation, we flag each sample with a non-thermal-overprint indicator recording which of the nine criteria it triggers. BIT and [2]/[3] screening in particular should be interpreted with caution. High BIT values are no longer interpreted uniformly across the TEX_{86} community as evidence of terrestrial input, since branched GDGTs can also be produced in situ in the water column (Peterse et al., 2009; Xiao et al., 2016), without necessarily biasing TEX_{86}-derived temperatures from marine isoGDGTs. The [2]/[3] ratio acts as a diagnostic tool to identify the contribution of deeper versus shallow-dwelling clades, an important metric to narrow down the choice of calibration (Van Der Weijst et al., 2022; Fokkema et al., 2024).

Finally, we recommend that users evaluate these non-thermal overprint flags critically in the context of their own research question, rather than discarding data based on a single criterion in isolation.

3.3 Miocene temperature calibration differences

3.3.1 Quantify calibration offsets

Different TEX_{86}-temperature calibrations may yield different absolute temperature values, and these differences can vary by region (Figure 3). We illustrate this using three representative sites from tropical, southern mid-latitude, and Antarctic regions: Sites U1488 (Figure 3a), 704 (Figure 3b), and U1356 (Figure 3c), respectively.

For Site U1488 (Figure 3a), SST estimates from the calibrations of Liu09, Kim10H, BAYSPAR, and O'Brien17 show little difference at low temperatures and a moderate difference of 2-4°C at high temperatures. Varma24 closely tracks these four calibrations at low temperatures but yields markedly warmer estimates at warmer temperatures. It exceeds BAYSPAR, the warmest of the four, by roughly 3-6°C at peak SST, making it the calibration with the largest high-temperature spread at this site. In contrast, SST estimates from the calibrations of Kim10L and DJ20 show unreasonably low temperature estimates compared to the other SST calibrations, with DJ20 producing the lowest estimates overall. The MioOcean UOT product closely tracks the Liu09/Kim10H/BAYSPAR/O'Brien17 group (differing by <1°C on average), sitting well above DJ20 and just below Varma24. Among three SubT calibrations by Kim12_0-200m, BAYSPAR_0-200m, and HL16_100-250m, BAYSPAR_0-200m generates the highest SubT, close to the estimates from BAYSPAR-SST. SubT estimates from Kim12_0-200m are lower than those from BAYSPAR_0-200m by ~6°C, and the estimates from HL16_100-250m are lower than those from Kim12_0-

https://doi.org/10.5194/essd-2026-711
Preprint. Discussion started: 2 November 2026
© Author(s) 2026. CC BY 4.0 License.



200m by ~6°C. The MioOcean SubT product closely tracks Kim12_0-200m, falling roughly midway between the higher BAYSPAR_0-200m and lower HL16_100-250m estimates.

At Site 704 (Figure 3b), SST calibrations converge after 6 Ma, except for DJ20 and Varma24, which remain toward the cooler end of the group. Prior to 6 Ma, the lowest SST estimates are from DJ20, followed by BAYSPAR-SST. Varma24 lies between this colder group and the warmer group formed by the remaining calibrations, which yield similar SST estimates to each other, except for Kim10L, which provides higher SST estimates prior to 15 Ma. The MioOcean UOT product closely tracks with the lower SST group (BAYSPAR-SST and DJ20), differing from DJ20 by <1°C on average. It therefore lies below the warmer SST group and below Varma24. SubT estimates from the three calibrations are comparable from approximately 15 Ma to the present. Prior to 15 Ma, HL16_100-250m yields the lowest SubT estimates, while the other two calibrations show similar SubT estimates. The MioOcean SubT product falls between the three SubT calibrations, tracking most closely with BAYSPAR_0-200m and HL16_100-250m while running slightly cooler than Kim12_0-200m.

At Site U1356 (Figure 3c), SST estimates obtained from Liu09 and O'Brien17 are similarly higher than those from BAYSPAR-SST and DJ20, which show similar lower SST estimates. SST estimates from Kim10L lie between these two groups but yield extremely higher SST values at peak temperatures. Varma24 also broadly follows Kim10L in magnitude but without the extreme peak SST values seen in Kim10L. The MioOcean UOT product closely tracks DJ20 and the lower SST group (BAYSPAR-SST, DJ20), running well below the higher group (Liu09, O'Brien17) as well as below Varma24 and Kim10L. SubT estimates from Kim12_0-200m are the highest, followed by those from HL16_100-250m. SubT estimates from BAYSPAR_0-200m are the lowest, close to the SST estimates from BAYSPAR-SST. The MioOcean SubT product falls between the three SubT calibrations, tracking most closely with HL16_100-250m while running warmer than BAYSPAR_0-200m and cooler than Kim12_0-200m.

3.3.2 Influence of calibration choice on comparisons among different sites or regions

The calibration choice has an impact on both the absolute magnitude of reconstructed and the apparent variability of regional temperature records through time. When using the BAYSPAR calibration, we observe a distinct offset between Site 982 in the North Atlantic (57.5°N; modern SST = 11.6°C) and Sites U1318 in the North Atlantic (51.2°N; modern SST = 12.6°C) and 882 in the North Pacific (50.4°N, modern SST = 5.5°C). In addition, BAYSPAR pronounces meridional gradient across the MMCT, with Southern Ocean sites appearing markedly colder than Northern Hemisphere high-latitude sites. In contrast, this gradient largely disappears when using the originally published SST values, which include BAYSPAR (Site 982), TEX^{L} (Site 882) and TEX^{H} (Site U1318) calibrations (Figure B1a,b).

Different calibrations can also lead to contrasting temperatures between broader regions, such as the tropics and subtropics. LOWESS-smoothed tropical and Subtropical reconstructions appear to be the same when applying the Kim10H calibration (Figure B1c,d). This similarity arises because the calibration effectively caps reconstructed temperatures at ~30ºC. Importantly, this limitation reflects the calibration rather than the proxy itself, as the TEX_{86} index has no intrinsic upper bound. By contrast,

https://doi.org/10.5194/essd-2026-711
Preprint. Discussion started: 2 November 2026
© Author(s) 2026. CC BY 4.0 License.



calibrations that allow warmer TEX_{86}-based estimates, such as the BAYSPAR (Tierney and Tingley, 2014), yield higher tropical than subtropical temperatures during the early and middle Miocene (Figure B1d,e). Even so, these tropical reconstructions are still likely underestimated, because warm pool records are sparse. Notably, our compilation shows that there are no published western tropical Pacific (WTP) reconstructions for the Early and Middle Miocene. This gap is likely caused by low organic carbon concentration or poor carbon preservation (Li et al., 2023). The lack of WTP records therefore limits our ability to constrain WTP temperatures during the Early and Middle Miocene.

In ice-proximal Antarctic regions (e.g. AND-2A, CRP-2, CIROS-1, McMurdo Erratics) the absolute temperature change strongly depends on the choice of calibration, but the resulting long and short term temperature trends are similar (Figure B1g,h). As such, while the calibrations continue to evolve in these regions, the results indicate that the general temperature trends are robust across calibrations.

To summarise, calibration choice can influence reconstructed temperatures and their spatial and temporal patterns. Independent temperature proxies can provide useful complementary constraints on these reconstructions and absolute temperatures, but differences among proxies should be interpreted in the context of their distinct environmental sensitivities, including habitat depth and seasonality. Where independent temperature proxy records are available (e.g., foraminiferal Mg/Ca, clumped isotopes, $U^{K}_{37'}$, Sosdian et al., this volume), they should be used to evaluate whether a given calibration yields reasonable reconstructions.

3.4 Miocene latitudinal temperature trends

In the tropics (0-20ºN/S), there are two temperature bands within the tropical SST stack (Figures 4b, B2a). Colder tropical temperatures are recorded from core sites in the eastern equatorial Pacific (Sites 850, 846, 1241), equatorial Atlantic (Sites 925, 667, 959) and sites in the Indian Ocean/Arabian Sea (Sites 730, 722). These sites are all located in upwelling areas or at least relatively close to such regions. In contrast, the warmer temperatures are recorded at sites from the western tropical Pacific (WTP) (Sites 1143, 1146, U1488, 806). The temperature difference between the WTP and the upwelling-related core sites in the Pacific, Atlantic and Indian Ocean is especially obvious in the Pliocene and Late Miocene, averaging ~3ºC and reaching up to ~5ºC in individual time intervals (Figure 5a). This gradient seems to be strongly reduced during the Early to Middle Miocene, however the data is more sparse in the Early Miocene, which may bias this conclusion.

There is high data coverage spatially and temporally for sites from the mid-latitude category (Figure 4c). Mid-latitude temperatures remain broadly flat from the Early Miocene through the MCO, with no clear evidence for a distinct warming trend into the MCO, followed by a modest cooling of only ca. 4ºC towards the present (Figure 5b). Similar to the low-latitude sites, colder temperatures are recorded from sites in upwelling areas like Site 467 in the California upwelling system and Site 1085 in the Benguela upwelling region (Figure B2b).

Due to differing trends, we divide the high latitude category into two hemispheric groups: "high latitude North" and "high latitude South" (Figure 4d and 4e). Within the northern high latitudes, we further distinguish transition sites, primarily located in the North Atlantic and influenced by the warm Gulf Stream, which makes them ~4-7ºC warmer than the other high-latitude

https://doi.org/10.5194/essd-2026-711
Preprint. Discussion started: 2 November 2026
© Author(s) 2026. CC BY 4.0 License.



Atlantic sites. In comparison, the high-latitude Pacific site (Site 882) seems to be consistently colder than the transition sites and high latitude North Atlantic sites (Figures 4d, 5c-g).

In the southern high latitudes, we distinguish among three groups: high-latitude Atlantic (Site 704), high-latitude Pacific (Sites 1168 and 1171), and Antarctic sites (Figure 5f-h). The high latitude Atlantic Site 704 is consistently colder than the Pacific sites located south of Tasmania, especially following the MMCT and Late Miocene cooling, resulting in an average temperature difference of up to 13ºC. This might be explained by the tectonic northward movement of the core sites or dynamic frontal migration in the Tasman Sea (Shevenell et al., 2004; Leutert et al., 2020; Hou et al., 2022). The separate Antarctic category includes sites >60ºS around the Antarctic continent (CRP-2, CIROS-1, AND-2A, McMurdo, U1356, 270, 274) (Figure 4e), characterized with uniquely different temperature trends compared to the open ocean South Atlantic and Southwest Pacific sites.

Because the depth at which GDGTs are exported remains uncertain, we examine the latitudinal structure of two TEX_{86}-based temperature products: the UOT and SubT. The Monte Carlo-derived UOT and SubT estimates bracket the plausible range of temperatures recorded by TEX_{86}. The latitudinal gradient recorded by MioOcean UOT and SubT differs substantially in magnitude (Figure B3). The equator-to-pole gradient in UOT (low latitude minus South Atlantic) is ~20–23°C and remains broadly consistent across the present, the MCO, and the full 0–25 Ma record. In contrast, the corresponding SubT gradient is roughly half as large (~10–14°C) over the same intervals, consistent with subsurface waters being comparatively well-mixed relative to the strong direct insolation control on surface temperatures at low latitudes. This compression of the gradient in SubT is not simply a uniform offset: at low latitudes UOT exceeds SubT by several degrees, as expected for surface waters warmer than the subsurface, but this relationship reverses at the high-latitude South Atlantic site (704), where SubT is consistently ~1–2°C warmer than UOT across the present, MCO, and full record. This sign reversal suggests that at high southern latitudes, sub-thermocline waters may be buffered against the strongest surface cooling recorded at the sea surface, though we note this pattern rests on the single Site 704 and warrants further investigation as more high-latitude SubT records become available.

3.5 Miocene temperature trends across ocean basins

In the Pacific Ocean, we observe three main temperature bands (Figure 6a): the western tropical Pacific (WTP), Eastern Equatorial Pacific (EEP), and North Pacific (N-Pacific) and Southwest Pacific (SW-Pacific) Ocean. The warmest temperature band is formed by records in the WTP (Sites 588, 769, 806, 811, 1143, 1146, QZ6 and U1488). The records from the EEP (Sites 846, 850 and 1241) are up to 6ºC colder than the WTP. Sites from the Tasman Sea (Sites 1168, 1171 and U1352) are up to ~12ºC colder than the WTP records, while the single North Pacific record (Site 882) is considerably colder still, up to ~20ºC colder than the WTP (Figure 6a). These two cold Pacific groups do not track each other as closely as their shared "cold" classification might suggest. The WTP sites show comparatively little change (~1ºC) between the late Miocene (5.3-11.6 Ma) and the MCO (14.7-16.9 Ma) (Figure 7a). In contrast, the SW-Pacific sites show a more modest cooling of ~2ºC between the

https://doi.org/10.5194/essd-2026-711
Preprint. Discussion started: 2 November 2026
© Author(s) 2026. CC BY 4.0 License.



MCO and late Miocene than previously estimated (Figure 7d). The EEP and N-Pacific sites lack MCO records to calculate the MCO-late Miocene cooling (Figure 7a-d).

In contrast to the Pacific Ocean, the Atlantic Ocean does not show a clear east-west temperature gradient, but rather exhibits distinct north-south temperature bands (Figure 6b). Equatorial Atlantic records (Sites 667, 925, 929 and 959) record the warmest temperatures. A Subtropical Atlantic group (Sites 516, 608, U1404 and U1406) records intermediate temperatures, these sites were reclassified out of the North Atlantic group because their paleo-warmth trend tracks the Subtropical rather than the high-latitude North Atlantic sites, despite their modern instrumental temperatures being closer to the latter. North Atlantic records (Sites 982 and U1318) are up to ~10ºC colder than the equatorial sites, and the South Atlantic record (Site 704) is the coldest among these groups. The pronounced temperature contrast between the equatorial, North and South Atlantic observed during the late Miocene appears to have developed after the MMCT (Figure 6b). The smallest temperature difference between MCO and the Late Miocene occurs at equatorial Atlantic sites (~4ºC) (Figure 7e). In contrast, the Subtropical, North and South Atlantic groups show stronger cooling of ~6ºC, ~2ºC and ~7ºC, respectively, with the South Atlantic sites experiencing the largest cooling among all MioTEX sites (Figure 7e-h).

In the Indian Ocean, temperature records from the Arabian Sea (Sites 722, 730 and U1457), central Indian Ocean (Site 754), western shelf of Australia (Sites U1461 and U1463), and the Mediterranean/Tethys (Agios Myron, Govone, Potamida, and Vicchio Formation) are broadly consistent and show cooling during the MMCT and late Miocene (Figure 6c). The largest cooling (~6ºC) is observed at the Mediterranean/Tethys sites, while the Arabian Sea and central Indian Ocean record more moderate cooling of ~4ºC and ~1ºC, respectively (Figure 7i, 7j, 6l), though all three of these MCO estimates rest on very few data points (n=4-6) and should be treated as preliminary until more MCO-age coverage is available.

Antarctic sites include sites located close to the continent (south of 60ºS using its paleolocation; CRP-2, CIROS-1, AND-2A, and McMurdo Erratics) and more offshore/distal sites (U1356, 270, and 274). Offshore/distal Site U1356 is warmer than the proximal sites prior to the MCO (~4ºC on average), but converges with the proximal sites' temperatures after the MCO, and remains close to the SSTs recorded in the South Atlantic (Site 704) throughout the record (Figure 4e). This offset is smaller but still present when alternative temperature calibrations are applied, with BAYSPAR and OPTiMAL yielding differences of ~3-5ºC. No clear long-term temperature trend is observed in the proximal sites across the Early, Middle and Late Miocene with the currently available dataset, partly due to the lack of Late Miocene records.

4 Conclusions and outlook

This compilation provides a global view of Miocene sea-surface temperatures reconstructed from TEX_{86}. It shows that the choice of calibration systematically affects the regional patterns and latitudinal gradients that emerge: several earlier calibrations were bounded by modern-ocean constraints and so unintentionally capped tropical reconstructions, whereas newer calibrations permit extrapolation above present-day temperatures, albeit with little experimental data in this warm range.

https://doi.org/10.5194/essd-2026-711
Preprint. Discussion started: 2 November 2026
© Author(s) 2026. CC BY 4.0 License.


Encouragingly, TEX_{86} is not saturated in the Miocene and has been applied successfully to hotter greenhouse climates such as the Eocene, so developing calibrations validated for warm conditions remains a high-value priority.

Despite two decades of development, no community-wide consensus exists on which SST or subT calibration best recovers absolute upper ocean temperatures. The underlying difficulty is that GDGTs are not produced exclusively at the mixed-layer depth, so any TEX_{86}-to-SST calibration embeds an implicit, and often incorrect, assumption about the offset between GDGT export depth and the mixed layer. Because this offset likely varied through time, among regions, and across major climate transitions, SST calibrations can yield systematically biased reconstructions wherever mixed-layer structure departed from that of the modern ocean. Many SST calibrations also overestimate temperature sensitivity at the warm end of the calibration range, amplifying high-temperature variability. TEX_{86}^{H} is a partial exception, as its exponential formulation flattens at high temperatures and may therefore be more suitable for reconstructing warm climates. For these reasons a growing number of studies favour SubT calibrations where GDGT production is thought to lie below the mixed layer, since these avoid assuming a fixed export-depth offset. The [2]/[3] ring ratio is a promising route to estimating production depth and could provide an objective, site- and interval-specific criterion for choosing between SST and SubT calibrations; southern high-latitude sites in particular may warrant a distinct strategy (Sect. 2.5.3). Complementary to such index-based approaches, mechanistic proxy system models that forward-model GDGT distributions rather than relying on empirical regressions, such as TEXAS (Rattanasriampaipong et al., 2026), offer a promising route to disentangling temperature from production-depth and other environmental controls, and to placing calibration selection on a more physiological footing. Incorporating OH-GDGTs in future work should further improve reconstructions, especially at high latitudes but also in the low and mid latitudes. Calibration is not the only source of uncertainty, however: non-thermal physiological controls also modulate the signal, as nutrient availability and ammonia-oxidation rates can alter archaeal GDGT distributions and elevate TEX_{86} independently of temperature (Rattanasriampaipong et al., 2025). Such effects are not captured by the screening indices applied here (BIT, methane index, and the ring-index and GDGT-ratio thresholds) and remain a still-unquantified source of bias, particularly for the warmest intervals.

Notwithstanding these calibration uncertainties, TEX_{86} has substantially advanced understanding of Miocene climate. Key findings from this upper ocean temperature compilation include:

- Relative to today, low latitudes were on average ~5°C warmer and mid latitudes ~8°C warmer during the MCO. Northern high latitudes warmed by ~9–11°C (North Atlantic +9°C; the 40–50°N transition zone +11°C, no MCO-age data exist yet for the North Pacific). Also southern high latitudes record generally warmer temperatures during MCO compared to today, from ~4°C at the Antarctic margin, to ~4°C in the South Atlantic, to ~9°C in the South Pacific.
- Within the tropical Pacific, the Western Tropical Pacific was ~3°C warmer than the eastern equatorial Pacific cold tongue through the Miocene, though it was comparable to, or slightly cooler than, low-latitude sites in the Atlantic and Indian Ocean.

https://doi.org/10.5194/essd-2026-711
Preprint. Discussion started: 2 November 2026
© Author(s) 2026. CC BY 4.0 License.


- Mid-latitude temperatures during the MCO were comparable to, or slightly warmer than, those of the early Miocene, with no clear evidence for an early Miocene temperature maximum. However, data are sparse (three sites) for the mid-latitude MCO.
- A distinct basinal asymmetry exists between the Atlantic and Pacific at high latitudes but with opposite sign in each hemisphere: the North Atlantic was ~13°C warmer than the North Pacific (Late Miocene, the only interval with data from both basins), while the South Pacific was ~8–13°C warmer than the South Atlantic (MCO to Late Miocene).

Closing the remaining gaps is now the main priority, both underrepresented regions (e.g. the South Atlantic, southern Indian Ocean, Antarctica) and underrepresented intervals (notably the Early Miocene). Part of this gap is intrinsic: low organic-carbon preservation in open-ocean MCO sediments limits data availability (Li et al., 2023). Broader spatial and temporal coverage would reduce the biases currently present in the dataset. To that end, we advocate standardized data templates, as used in MioTEX and the community framework of Bijl, Śliwińska et al. (2025), together with transparent reporting of null results and barren samples, which is essential for gauging sampling limitations and dataset completeness. No single proxy is without limitations, and clear communication of those limitations is what makes multi-proxy synthesis powerful, as demonstrated by the MioOcean initiative, whose collaborative, multi-proxy framework strengthens the reliability of Miocene climate reconstructions and provides a foundation for future work.

https://doi.org/10.5194/essd-2026-711
Preprint. Discussion started: 2 November 2026
© Author(s) 2026. CC BY 4.0 License.

Open Access Earth System Science Data Discussions

Figures

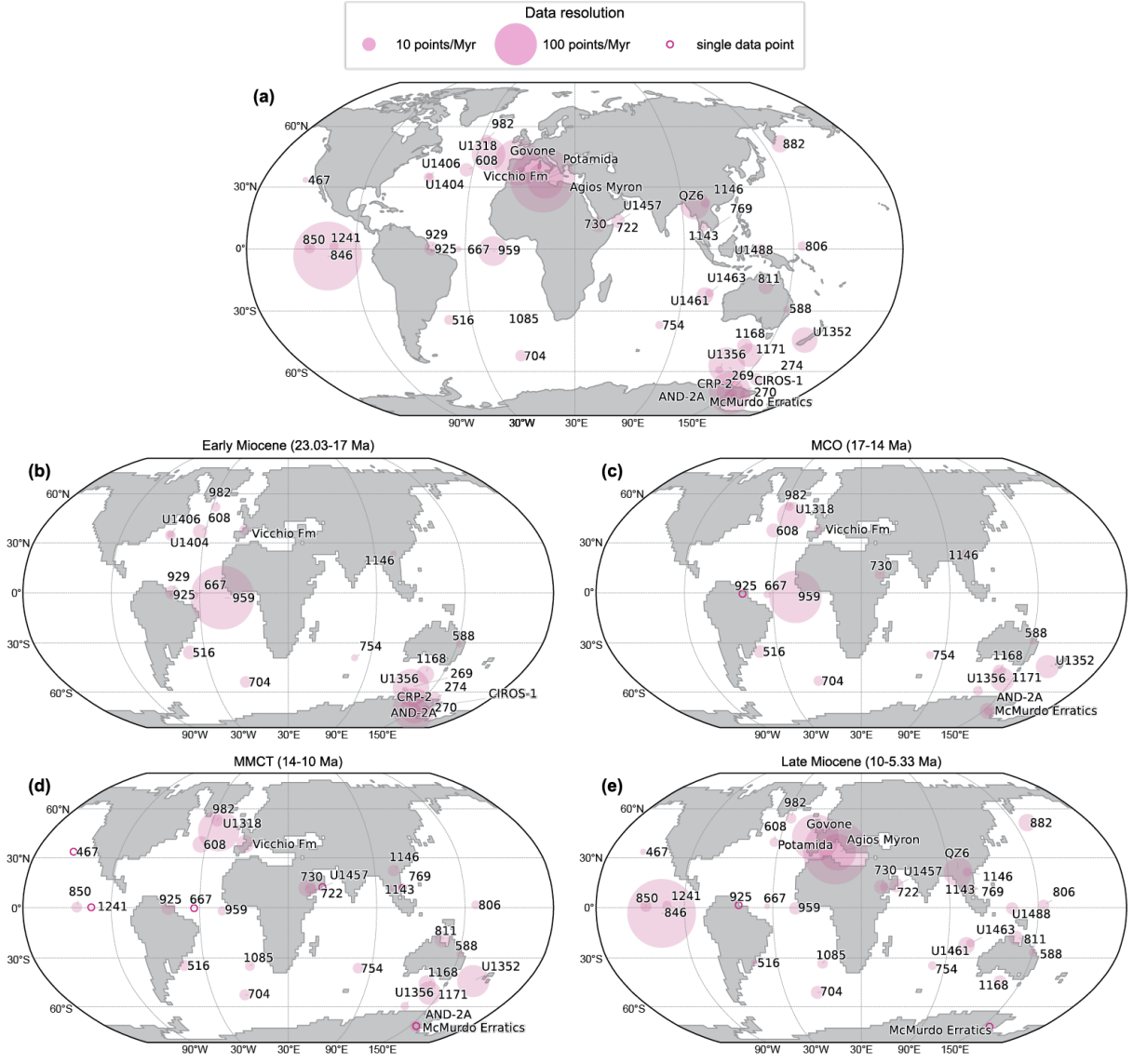


Figure 1 Core sites included in the MioTEX compilation. (a) all MioTEX sites on a map of modern geography. (b), (c), (d) and (e) show the sites of the early Miocene (23.03-17 Ma), Miocene Climate Optimum (17-14 Ma), Middle Miocene Climate Transition (14-10 Ma) and late Miocene (10-5.33 Ma) on a map of Miocene paleogeography from Burls et al. (2026), respectively. The site locations in (b)–(e) represent reconstructed paleopositions, with paleocoordinates calculated as the mean of the oldest and youngest reconstructed positions within each interval. Larger filled circles indicate higher data resolution (i.e., more data points per million years), whereas hollow circles indicate sites with only a single data point available during an interval.

https://doi.org/10.5194/essd-2026-711
Preprint. Discussion started: 2 November 2026
© Author(s) 2026. CC BY 4.0 License.

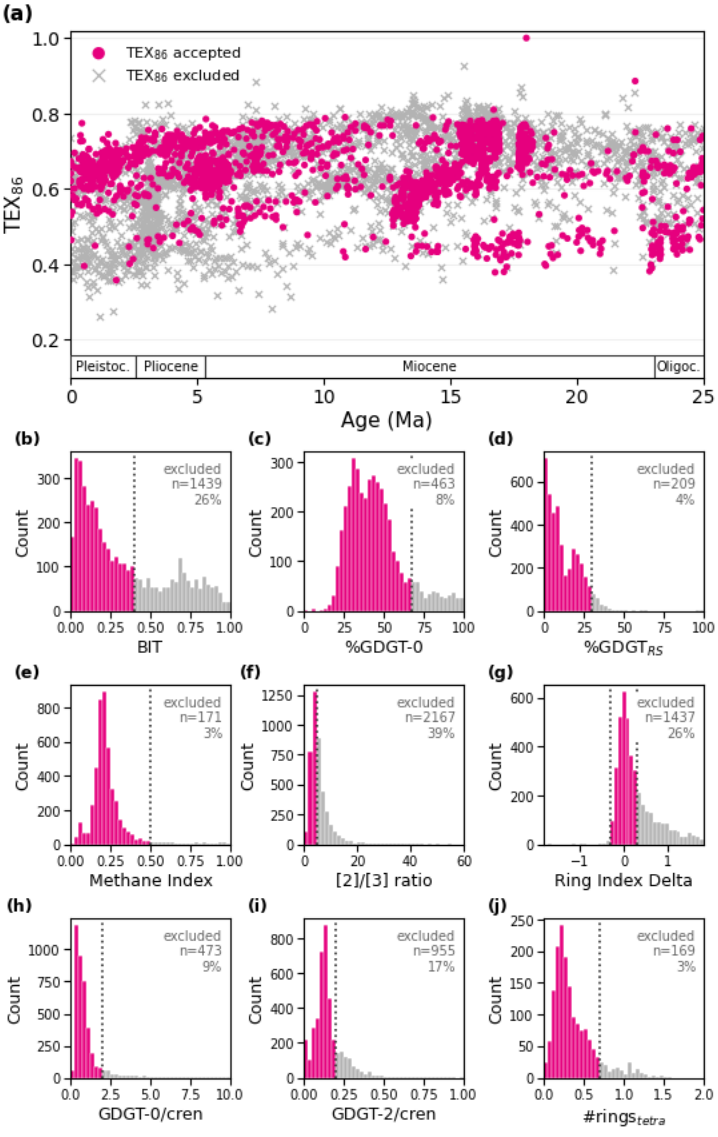


Figure 2 Screening criteria for non-thermal influences on TEX_{86}-derived temperatures. (a) All accepted and excluded TEX_{86} data based on excluding criteria (Table A2). (b) BIT and number of data excluded. Percentage of data excluded for data with BIT values and percentage of data excluded compared to total datapoints. (c) %GDGT-0. (d) $\%GDGT_{RS}$. (e) methane index. (f) [2]/[3] ratio. (g) ring index delta. (h) GDGT-0/cren. (i) GDGT-2/cren. (j) $\#rings_{tetra}$.

https://doi.org/10.5194/essd-2026-711
Preprint. Discussion started: 2 November 2026
© Author(s) 2026. CC BY 4.0 License.



Open Access Earth System Science Data Discussions

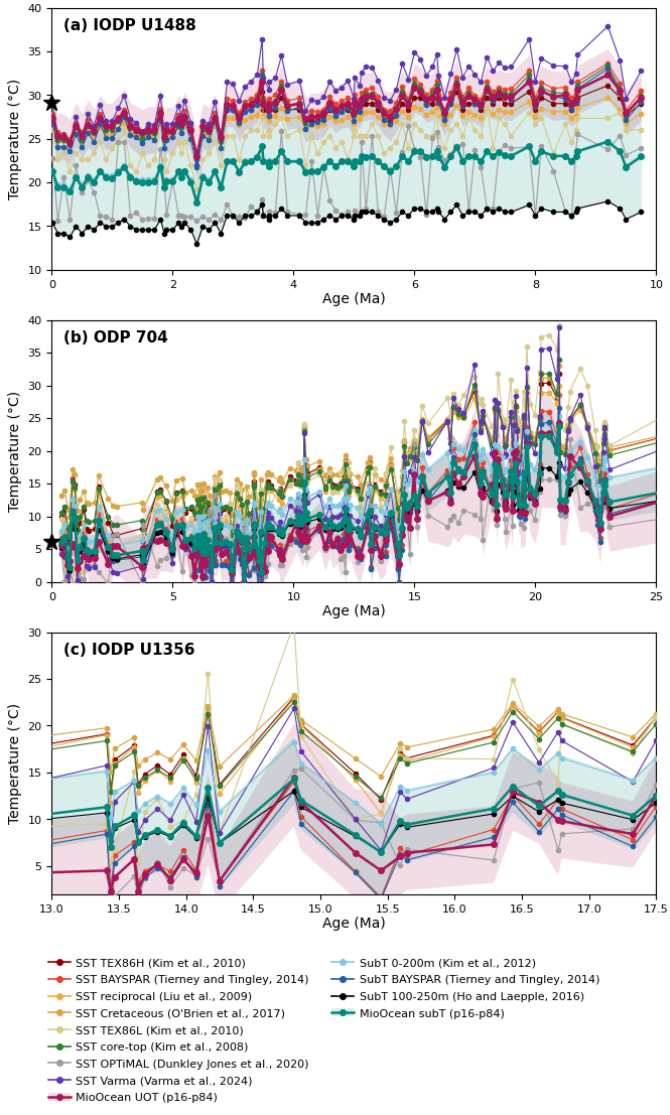


Figure 3 Calculated calibrations for core sites (a) IODP U1488, (b) ODP 704, and (c) IODP U1356. Thick lines show the MioOcean UOT (berry) and MioOcean SubT (teal) products, with shaded bands giving the p16-p84 uncertainty range; thin lines show the individual published calibrations they are derived from. Black stars in (a) and (b) mark each site's modern instrumental temperature. The temperatures reported in the original publications were calculated with BAYSPAR SST (Tierney & Tingley, 2014) for U1488 (Liu et al., 2022) and ODP 704 (Auderset et al., 2022), and with the TEX_{86} linear calibration (0 m; Kim et al., 2010) for U1356 (Hartman et al., 2018). Note the large calibration-driven temperature offsets, commonly exceeding 10 °C and reaching up to ~24 °C at some intervals. Calibrations used for comparison are listed in Table A3.

https://doi.org/10.5194/essd-2026-711
Preprint. Discussion started: 2 November 2026
© Author(s) 2026. CC BY 4.0 License.

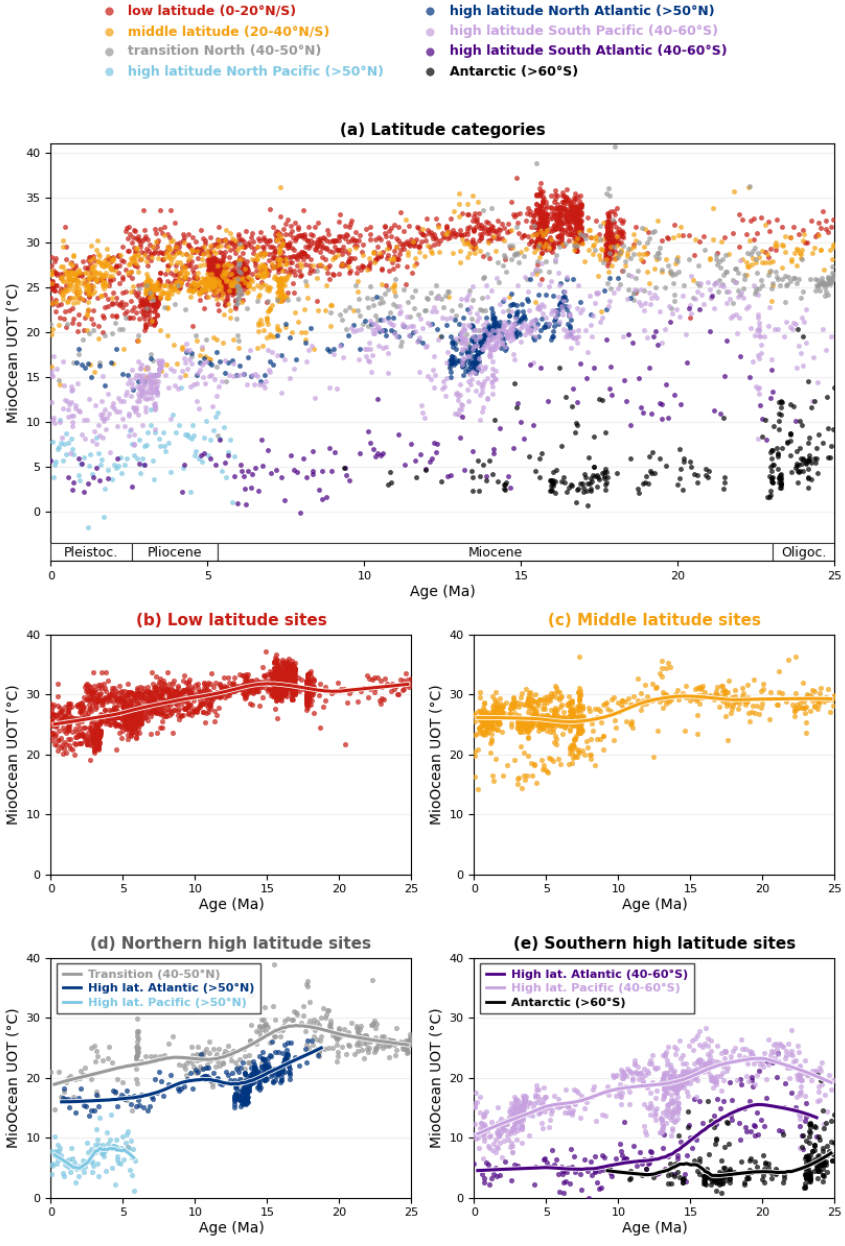


Figure 4 (a) Categorised MioTEX compilation based on latitude, using MioOcean upper ocean temperature (UOT). (a) All sites, colored by latitude category. Solid curves in (b)-(e) show LOWESS-smoothed trends (0.5 Myr age bins, local-linear span = 0.4 of the bins). (b) Low latitude sites (0-20°N/S). (c) Middle latitude sites (20-40°N/S). (d) High latitude North Pacific (light blue) and North Atlantic (dark blue) sites (>50°N), and transition sites between middle and high northern latitudes (40-50°N, grey). (e) High latitude South Pacific (light purple) and South Atlantic (dark purple) sites (40-60°S), and sites close to Antarctica (>60°S).

https://doi.org/10.5194/essd-2026-711
Preprint. Discussion started: 2 November 2026
© Author(s) 2026. CC BY 4.0 License.

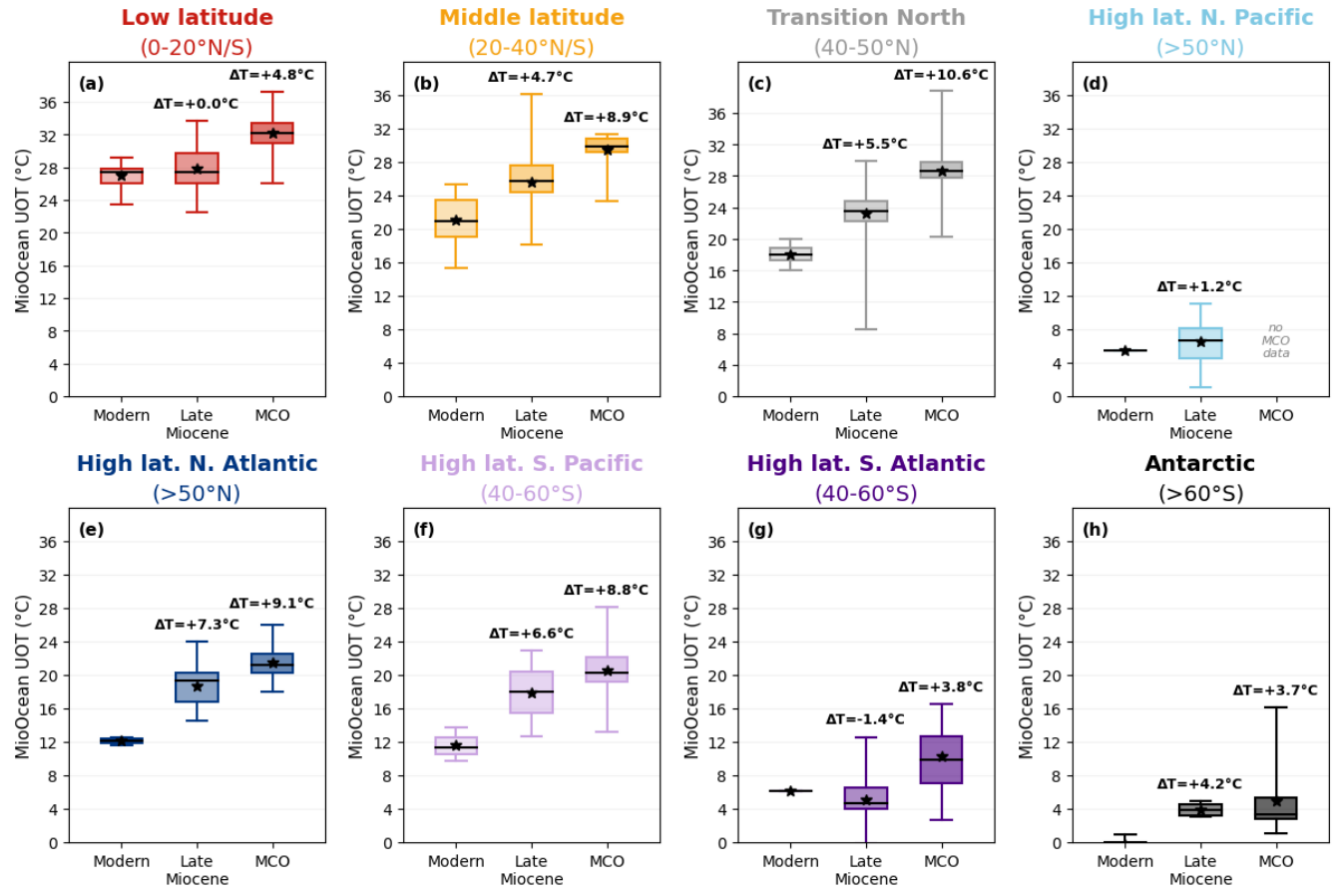


Figure 5 MioOcean UOT (upper ocean temperature) distributions by latitude band, comparing Modern instrumental temperatures against two Miocene time slices: the Late Miocene (5.3–11.6 Ma) and the Miocene Climatic Optimum (MCO, 14.7–16.9 Ma). Sites are grouped by modern latitude following the same classification as Figure 4: (a) low latitude (0–20°N/S), (b) middle latitude (20–40°N/S), (c) transition North (40–50°N), (d) high-latitude North Pacific (>50°N), (e) high-latitude North Atlantic (>50°N), (f) high-latitude South Pacific (40–60°S), (g) high-latitude South Atlantic (40–60°S), and (h) Antarctic (>60°S). Boxes show the interquartile range, the horizontal line the median, whiskers the full data range, and the black star the mean. ΔT values give the change in median UOT relative to the modern median for each time slice. Panel (d) lacks MCO data because its only contributing site (882) has no Miocene-age coverage.

https://doi.org/10.5194/essd-2026-711
Preprint. Discussion started: 2 November 2026
© Author(s) 2026. CC BY 4.0 License.

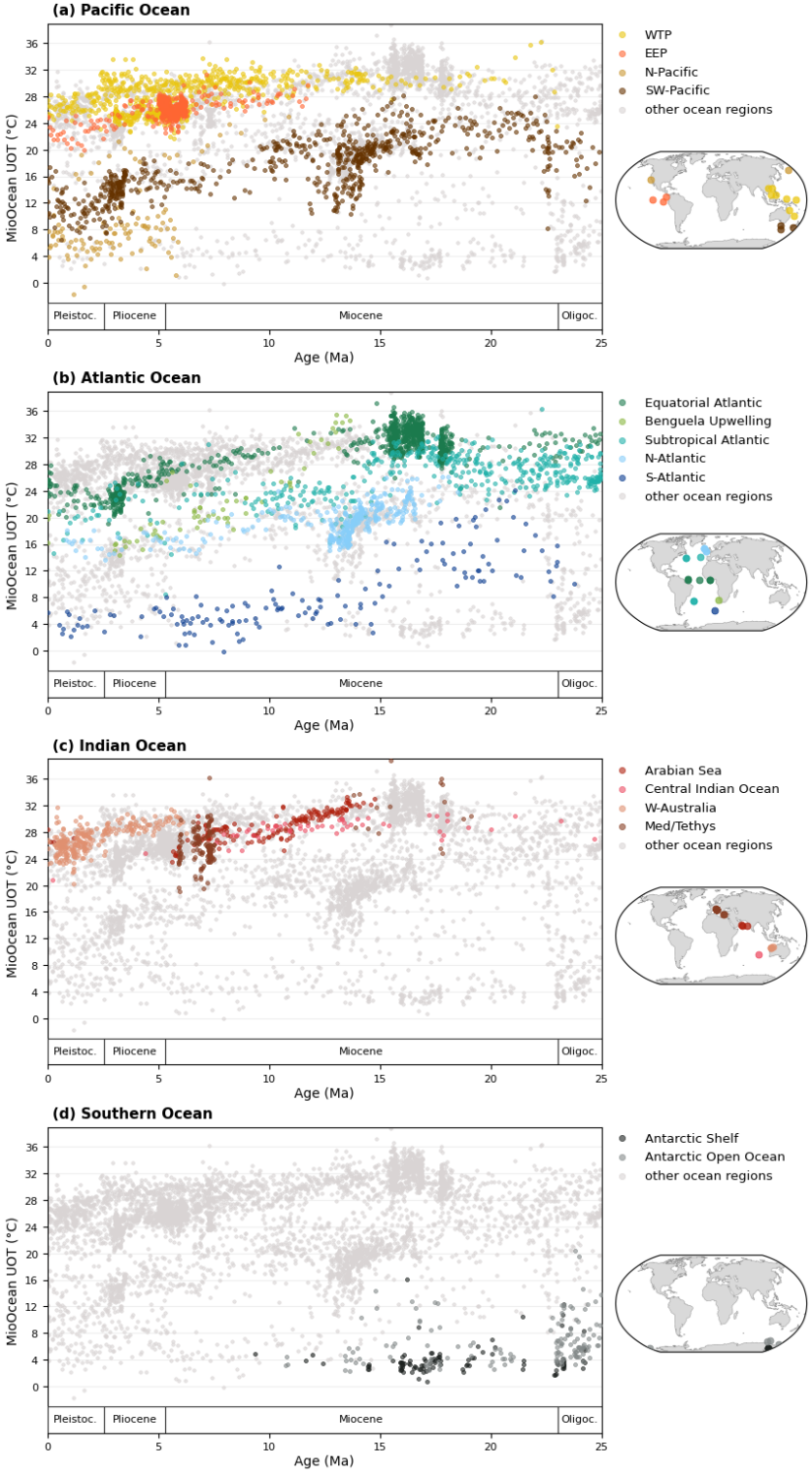


Figure 6 MioOcean upper ocean temperature (UOT) for the categorised MioTEX compilation, grouped by ocean basin and region and plotted against MioOcean-derived age. (a) Pacific Ocean is divided into the West Pacific Warm Pool (WPWP), Eastern Equatorial Pacific (EEP), North Pacific (N-Pacific), and Southwest Pacific (SW-Pacific; Tasman Sea and New Zealand). (b) Atlantic Ocean is divided into Equatorial Atlantic, Benguela Upwelling, Subtropical Atlantic, North Atlantic (N-Atlantic), and South Atlantic (S-Atlantic). (c) Indian Ocean is divided into Arabian Sea, Central Indian Ocean, Western Australian shelf (W-Australia), and the Mediterranean/Tethys region (Med/Tethys). (d) Southern Ocean sites are divided into Antarctic Shelf and Antarctic Open Ocean sites. A list of all sites within each ocean basin and region can be found in Table A1.

https://doi.org/10.5194/essd-2026-711
Preprint. Discussion started: 2 November 2026
© Author(s) 2026. CC BY 4.0 License.

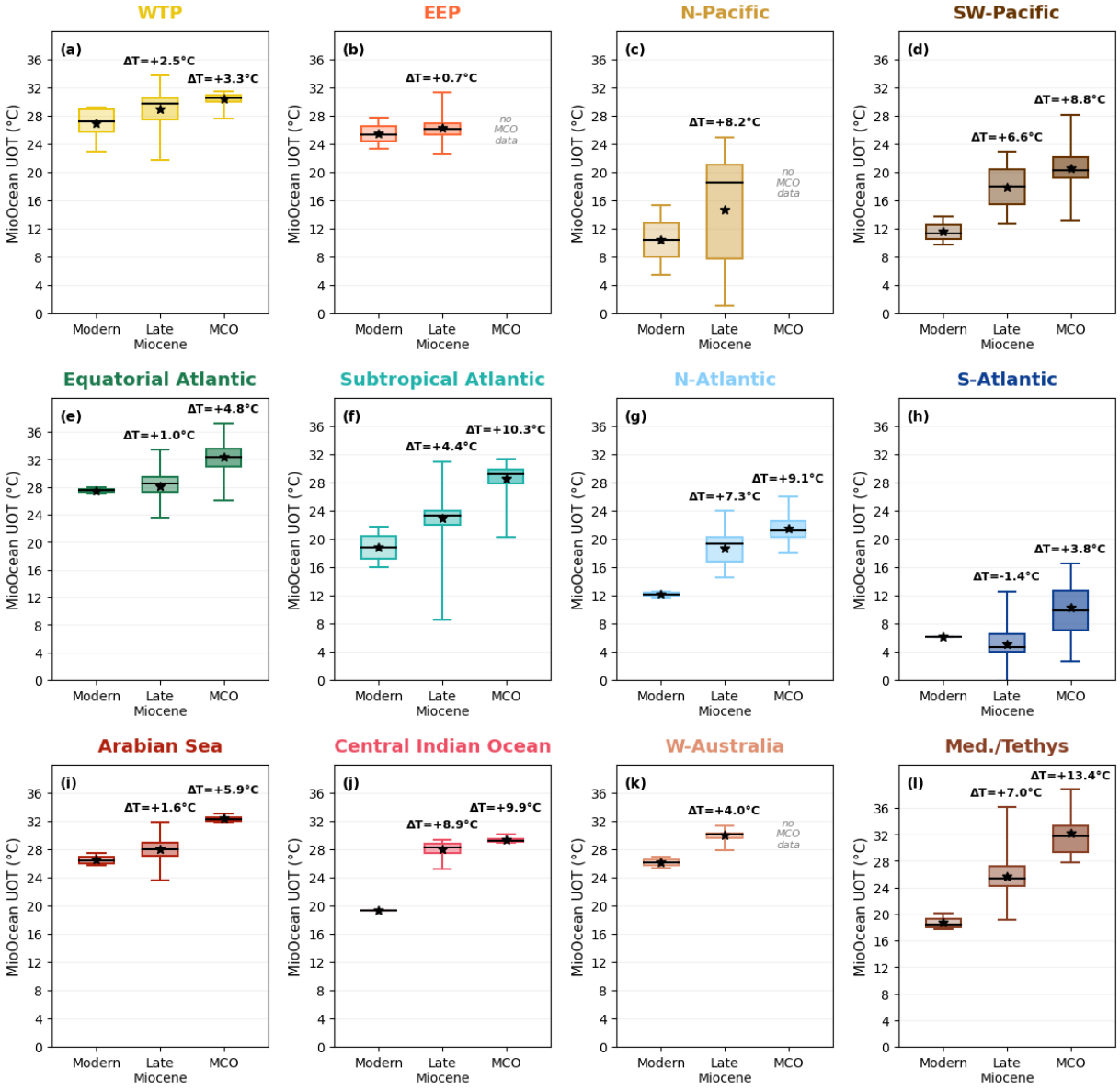


Figure 7 Temperature difference between MCO (14.7–16.9 Ma) and Late Miocene (5.3–11.6 Ma) based on MioOcean upper ocean temperature (UOT) and MioOcean-derived age. (a) Western Tropical Pacific (WTP) Sites 588, 769, 806, 811, 1143, 1146, U1488, QZ6, (b) Eastern Equatorial Pacific Sites 846, 850, 1241, (c) North Pacific Site 882, (d) Southwest Pacific Sites 1168, 1171, U1352, (e) Equatorial Atlantic Sites 667, 925, 959, (f) Benguela Upwelling Site 1085, (g) Subtropical Atlantic Sites 516, 608, (h) North Atlantic Sites 982, U1318, (i) South Atlantic Site 704, (j) Arabian Sea Sites 722, 730, U1457, (k) Central Indian Ocean Site 754, (l) Western Australian Sites U1461, U1463, (m) Mediterranean/Tethys Sites Agios Myron, Govone, Potamida, Vicchio Fm. Not plotted as a separate box plot are the Atlantic upwelling site 1085 and Antarctic sites. A list of all sites within the specific ocean basins and regions can be found in Table A1.

https://doi.org/10.5194/essd-2026-711
Preprint. Discussion started: 2 November 2026
© Author(s) 2026. CC BY 4.0 License.



Open Access Earth System Science Data Discussions

Appendix A - Tables

Table A1 - List of temperature records used for MioTEX compilation.

Site	Basin	Shelf vs. Open ocean	Region	Modern Long.	Modern Lat.	Age Start (Ma)	Age Stop (Ma)	Reso-lution (kyr)	#sample	Reference	Published calibration	Monte Carlo choice
269	Southern Ocean	Open ocean	Distal/ Offshore Antarctic	140.10	-61.68	22.98	24.18	80	15	Evangelinos et al. (2020)	TEX_{86} linear calibration model 0m (Kim et al., 2010)	High latitude
270	Southern Ocean	Open ocean	Distal/ Offshore Antarctic	-178.50	-77.44	19.98	25.44	156	35	Duncan et al. (2022)	OPTiMAL SST (Dunkley Jones et al., 2020)	High latitude
274	Southern Ocean	Open ocean	Distal/ Offshore Antarctic	173.43	-69.00	17.11	18.50	126	12	Duncan et al. (2022)	OPTiMAL SST (Dunkley Jones et al., 2020)	High latitude
467	Pacific Ocean	Open ocean	North Pacific	33.8495	-120.758	0.29	10.87	460	23	Witkowski et al. (2024)	TEXH SST (Kim et al., 2010)	Low latitude
516	Atlantic Ocean	Open ocean	Subtropical Atlantic	-35.29	-30.28	6.05	73.40	315	290	(Auderset et al., 2022; O'brien et al., 2020)	BAYSPAR SST (Tierney and Tingley, 2014)	Low latitude
588	Pacific Ocean	Open ocean	Western Tropical Pacific	161.23	-26.11	0.00	23.00	451	51	Auderset et al. (2022)	BAYSPAR SST (Tierney and Tingley, 2014)	Low latitude
608	Atlantic Ocean	Open ocean	Subtropical Atlantic	-23.09	42.84	0.00	26.95	108	207	(Super et al., 2020; Super et al., 2018)	BAYSPAR SST (Tierney and Tingley, 2014)	Low latitude
667	Atlantic Ocean	Open ocean	Equatorial Atlantic	-21.91	4.57	0.00	22.42	628	37	Auderset et al. (2022)	BAYSPAR SST (Tierney and Tingley, 2014)	Low latitude
704	Atlantic Ocean	Open ocean	South Atlantic	7.42	-46.88	0.41	27.51	182	156	Auderset et al. (2022)	BAYSPAR SST (Tierney and Tingley, 2014)	High latitude
722	Indian Ocean	Open ocean	Arabian Sea	59.80	16.62	7.06	13.50	259	32	Zhuang et al. (2017)	BAYSPAR SST (Tierney and Tingley, 2014)	Low latitude
730	Indian Ocean	Open ocean	Arabian Sea	57.69	17.73	0.01	14.76	260	80	(Auderset et al., 2022; Zhuang et al., 2017)	BAYSPAR SST (Tierney and Tingley, 2014)	Low latitude
754	Indian Ocean	Open ocean	Central Indian Ocean	93.60	-30.90	0.25	28.35	551	56	Auderset et al. (2022)	BAYSPAR SST (Tierney	Low latitude

https://doi.org/10.5194/essd-2026-711
Preprint. Discussion started: 2 November 2026
© Author(s) 2026. CC BY 4.0 License.



											and Tingley, 2014)	
769	Pacific Ocean	Open ocean	Western Tropical Pacific	121.29	8.79	2.80	11.25	1207	7	Zhang et al. (2014)	Global core-top calibration model (0 m) (Kim et al., 2008)	Low latitude
806	Pacific Ocean	Open ocean	Western Tropical Pacific	159.36	0.32	0.07	12.72	132	90	Zhang et al. (2014)	Global core-top calibration model (0 m) (Kim et al., 2008)	Low latitude
811	Pacific Ocean	Open ocean	Western Tropical Pacific	148.16	-16.52	1.93	11.05	85	107	Petrick et al. (2023)	TEXH SST (Kim et al., 2010)	Low latitude
846	Pacific Ocean	Open ocean	Eastern Equatorial Pacific	-90.82	-3.10	5.02	6.25	3	334	Lawrence et al. (2020)	Global core-top calibration model (0 m) (Kim et al., 2008)	Low latitude
850	Pacific Ocean	Unknown	Eastern Equatorial Pacific	-110.52	1.30	0.00	11.76	149	80	Zhang et al. (2014)	Global core-top calibration model (0 m) (Kim et al., 2008)	Low latitude
882	Pacific Ocean	Open ocean	North Pacific	167.60	50.36	0.04	5.87	62	94	Yamamoto and Kobayashi (2016)	TEXL SST (Kim et al., 2010)	High latitude
925	Atlantic Ocean	Open ocean	Equatorial Atlantic	-43.49	4.20	0.01	39.35	449	86	Zhang et al. (2013)	Reciprocal calibration (Liu et al., 2009)	Low latitude
929	Atlantic Ocean	Open ocean	Equatorial Atlantic	-43.74	5.98	21.94	29.78	102	81	O'brien et al. (2020)	BAYSPAR SST (Tierney and Tingley, 2014)	Low latitude
959	Atlantic Ocean	Open ocean	Equatorial Atlantic	-2.74	3.63	0.00	18.25	6	787	(Wubben et al., 2024; Van Der Weijst et al., 2022)	TEXH SST (Kim et al., 2010)	Low latitude
982	Atlantic Ocean	Open ocean	North Atlantic	-15.87	57.52	0.82	18.50	176	100	Super et al. (2020)	BAYSPAR SST (Tierney and Tingley, 2014)	High latitude
1085	Atlantic Ocean	Open ocean	Upwelling Atlantic	13.99	-29.37	0.02	13.63	207	66	Rommerskirchen et al. (2011)	TEXH SST (Kim et al., 2010)	Low latitude
1143	Pacific Ocean	Open ocean	Western Tropical Pacific	113.29	9.36	2.86	10.84	164	49	Zhang et al. (2014)	Global core-top calibration model (0 m) (Kim et al., 2008)	Low latitude

https://doi.org/10.5194/essd-2026-711
Preprint. Discussion started: 2 November 2026
© Author(s) 2026. CC BY 4.0 License.



1146	Pacific Ocean	Open ocean	Western Tropical Pacific	116.27	19.46	0.00	20.67	255	76	Auderset et al. (2022)	BAYSPAR SST (Tierney and Tingley, 2014)	Low latitude
1168	Southern Ocean	Open ocean	Tasmania and New Zealand	144.41	-42.61	0.02	35.00	52	581	(Hoem et al., 2022; Hou et al., 2023)	BAYSPAR SST (Tierney and Tingley, 2014); Whole-column temperature calibration (He et al., 2021)	High latitude
1171	Southern Ocean	Open ocean	Tasmania and New Zealand	149.11	-48.50	11.76	15.48	32	115	Leutert et al. (2020)	TEXH SST (Kim et al., 2010)	High latitude
1241	Pacific Ocean	Open ocean	Eastern Equatorial Pacific	-86.44	5.84	0.09	10.12	197	48	Seki et al. (2012)	TEXH SST (Kim et al., 2010)	Low latitude
Agios Myron	Atlantic Ocean	Unknown	Tethys/ Mediterranean	25.22	35.39	6.54	7.17	13	47	Kontakiotis et al. (2022)	TEXH SST (Kim et al., 2010)	Low latitude
AND-2A	Southern Ocean	Shelf	Proximal Antarctic	165.28	-77.76	11.65	20.20	132	70	Levy et al. (2016)	TEXL subT 0-200m (Kim et al., 2012)	High latitude
CIROS-1	Southern Ocean	Shelf	Proximal Antarctic	164.50	-77.08	22.86	36.00	268	53	Duncan et al. (2022)	OPTiMAL SST (Dunkley Jones et al., 2020)	High latitude
CRP-2	Southern Ocean	Shelf	Proximal Antarctic	163.72	-77.01	21.44	24.26	217	14	Duncan et al. (2022)	OPTiMAL SST (Dunkley Jones et al., 2020)	High latitude
Govone	Atlantic Ocean	Unknown	Tethys/ Mediterranean	8.13	44.80	5.92	6.09	12	21	Sabino et al. (2021)	*N/A*	Low latitude
McMurdo Erratics	Southern Ocean	Unknown	Proximal Antarctic	166.66	-77.85	9.36	43.90	3454	14	Duncan et al. (2022)	OPTiMAL SST (Dunkley Jones et al., 2020)	High latitude
Potamida	Atlantic Ocean	Unknown	Tethys/ Mediterranean	23.70	35.47	7.21	7.51	7	72	Besiou et al. (2024)	TEXH SST (Kim et al., 2010)	Low latitude
QZ6	Pacific Ocean	Shelf	Western Tropical Pacific	109.80	20.20	3.02	6.42	17	212	Wang et al. (2021)	TEXH SST (Kim et al., 2010)	Low latitude
U1318	Atlantic Ocean	Open ocean	North Atlantic	-11.55	51.44	12.54	16.57	16	243	Sangiorgi et al. (2021)	TEXH SST (Kim et al., 2010)	Low latitude
U1352	Pacific Ocean	Shelf	Tasmania and New Zealand	172.02	-44.94	13.07	16.83	27	138	Herbert et al. (2022)	TEXH SST (Kim et al., 2010)	High latitude

https://doi.org/10.5194/essd-2026-711
Preprint. Discussion started: 2 November 2026
© Author(s) 2026. CC BY 4.0 License.



U1356	Southern Ocean	Open ocean	Distal/ Offshore Antarctic	136.00	-63.31	10.77	34.82	155	145	Hartman et al. (2018)	TEX_{86} linear calibration model (0m) (Kim et al., 2010)	High latitude
U1404	Atlantic Ocean	Open ocean	Subtropical Atlantic	-51.81	40.01	18.43	42.87	69	358	Wang et al. (2023)	*N/A*	Low latitude
U1406	Atlantic Ocean	Open ocean	Subtropical Atlantic	-51.65	40.35	18.00	29.53	385	28	Guitián et al. (2019)	BAYSPAR SST (Tierney and Tingley, 2014)	Low latitude
U1457	Indian Ocean	Open ocean	Arabian Sea	67.93	17.17	5.71	10.12	90	49	Feakins et al. (2020)	BAYSPAR subT (Tierney and Tingley, 2014)	Low latitude
U1461	Indian Ocean	Shelf	Eastern Indian Ocean	115.07	-20.21	0.01	6.08	28	233	He et al. (2021)	Whole-column temperature calibration (He et al., 2021)	Low latitude
U1463	Indian Ocean	Shelf	Eastern Indian Ocean	117.62	-18.97	0.45	6.25	341	17	Christensen et al. (2017)	BAYSPAR SST (Tierney and Tingley, 2014)	Low latitude
U1488	Pacific Ocean	Open ocean	Western Tropical Pacific	141.75	2.04	0.01	9.75	104	95	Liu et al. (2022)	BAYSPAR SST (Tierney and Tingley, 2014)	Low latitude
Vicchio Fm	Atlantic Ocean	Unknown	Tethys/ Mediterranean	11.50	43.93	13.80	19.09	331	16	Salocchi et al. (2021)	TEXH SST (Kim et al., 2010)	Low latitude

https://doi.org/10.5194/essd-2026-711
Preprint. Discussion started: 2 November 2026
© Author(s) 2026. CC BY 4.0 License.



Open Access Earth System Science Data Discussions

Table A2 - Screening criteria to minimize the effect of non-thermal factors on GDGT distributions and TEX_{86}-based temperature estimates

Index	Description	Equation	Exclusion threshold	Reference	Application in MioTEX
BIT	Branched vs. Isoprenoid Tetraether Index terrestrial input/ proportion of brGDGTs *versus* isoGDGTs (cren)	BIT = (brGDGT-I+brGDGT-II+brGDGT-III)/(brGDGT-1+brGDGT-II+brGDGT-III+cren)	BIT > 0.4	Hopmans et al. (2004)	if applied, 26.2% of samples removed
#ringstetra	#ringstetra sources of terrestrial brGDGTs	#ringstetra = (brGDGT-Ib + 2 * brGDGT-Ic) / (brGDGT-Ia + brGDGT-Ib + brGDGT-Ic)	#ringstetra > 0.7	Sinninghe Damsté (2016)	if applied, 2.7% of samples removed; if combined with BIT, 1.2% of samples removed
MI	Methane Index anaerobic methane oxidation	MI = (isoGDGT1I + isoGDGT-2 + isoGDGT-3) / (isoGDGT-1 + isoGDGT-2 + isoGDGT-3 + cren + cren')	MI > 0.3-0.5	Zhang et al. (2011)	if applied (>0.5), 3.1% of samples removed
%GDGT-0	%GDGT-0 methanogenesis	%GDGT-0 = (isoGDGT-0 / (isoGDGT-0 + cren)) * 100	%GDGT-0 > 67%	Sinninghe Damsté et al. (2012)	if applied, 8.4% of samples removed
GDGT-0/Cren	GDGT-0/Cren methanogenesis	GDGT-0/Cren = isoGDGT-0 / cren	GDGT-0/Cren > 2	Blaga et al. (2009)	if applied, 9.2% of samples removed
GDGT-2/Cren	ANME	isoGDGT-2 / cren	GDGT-2/Cren >0.2	Weijers et al. (2011)	if applied, 17.4% of samples removed
[2/3] ratio	[2/3] ratio water depth of production	[2/3] = isoGDGT-2 / isoGDGT-3	[2/3] ratio > 5	Taylor et al. (2013), Hernandez-Sanchez et al. (2014) Hurley et al. (2018)	if applied, 39.4% of samples removed
RI	Ring Index anomalous GDGT distribution	RI = (0×[GDGT-0] + 1×[GDGT-1] + 2×[GDGT-2] + 3×[GDGT-3] + 4×[GDGT-4] + 4×[cren] + 4×[cren']) / ([GDGT-0] + [GDGT-1] + [GDGT-2] + [GDGT-3] + [GDGT-4] + [cren] + [cren']) ΔRI = RI observed - RI predicted RI_predicted = $-2.008 \times (TEX86)^2 + 3.555 \times TEX86 + 0.263$	-0.3 > DRI > 0.3	Zhang et al. (2016)	if applied, 26.1% of samples removed
$\%GDGT_{RS}$	Red Sea type GDGTs anomalous GDGT distribution	$\%GDGT_{RS}$ = (cren' / (isoGDGT-0 + cren')) * 100	%GDGTRS > 30	Inglis et al. (2015)	if applied, 3.8% of samples removed

https://doi.org/10.5194/essd-2026-711
Preprint. Discussion started: 2 November 2026
© Author(s) 2026. CC BY 4.0 License.



Open Access Earth System Science Data Discussions

Table A3 - Sea surface and subsurface temperature calibrations compared for the MioTEX compilation

Index/name	SST/SubT	Equation	Uncertainty	Reference
TEX^{H}	SST	SST = 68.4 * TEXH + 38.6	RSE ±2.5°C	Kim et al. (2010)
TEX^{L}	SST	SST = 67.5 * TEXL + 46.9	RSE ±4.0°C	Kim et al. (2010)
TEX linear	SST	SST = 50.2 * TEXH + 42.0	RSE ±3.4°C	Kim et al. (2010)
global core top (0m)	SST	SST = 56.2 * TEX − 10.78	RSE ±1.7°C	Kim et al. (2008)
BAYSPAR-SST	SST	Matlab code	90th percent confidence intervals	Tierney and Tingley (2014)
OPTiMAL	SST	Matlab code	RMSE ±3.6°C	Dunkley Jones et al. (2020)
Liu reciprocal	SST	SST = -16.332 * (1/TEX) + 50.475	68.2% confidence interval, RSE not reported	Liu et al. (2009)
O'Brien linear	SST	SST = 47.7 * TEX − 5	RSE ±2.0°C	O'Brien et al. (2017)
Varma	SST	SST = (TEX86 − 0.33) / 0.012	not reported	Varma et al. (2024)
SubT 0-200m	SubT	SubT = 54.7 * TEXH + 30.7	RSE ±2.2°C	Kim et al. (2012)
BAYSPAR-SubT	SubT	Matlab code	90th percent confidence intervals	Tierney and Tingley (2014)
Ho&Laepple SubT 100-250m	SubT	SubT = 40.8 * TEXH + 22.3	RSE ±1.4°C	Ho and Laepple (2016)
whole column temperature calibration	whole water column	T = 58.44 * TEX − 17.04	not reported	He et al. (2021)

https://doi.org/10.5194/essd-2026-711
Preprint. Discussion started: 2 November 2026
© Author(s) 2026. CC BY 4.0 License.



Open Access Earth System Science Data Discussions

Appendix B – Additional Figures

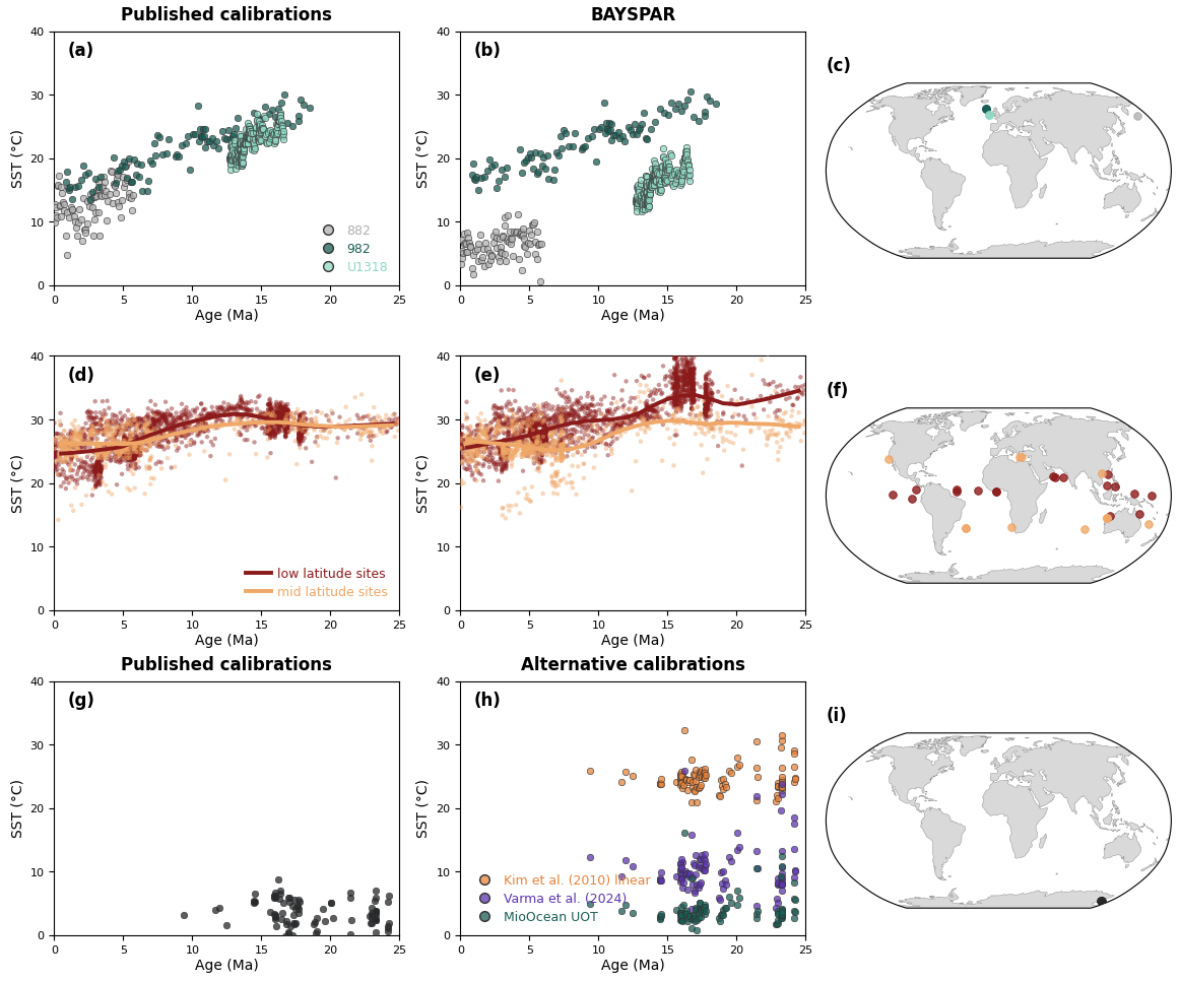


Figure B1 Calibration choice alters both site-level temperature offsets and regional temperature contrasts. (a–b) SST at high-latitude Sites 882 (North Pacific), 982, and U1318 (North Atlantic) using **(a)** published calibrations (BAYSPAR, TEX^{L}, or TEX^{H}, as originally reported per site) versus **(b)** BAYSPAR recalculated uniformly for all three sites; **(c)** map of site locations. (d–e) LOWESS-smoothed SST for low- and mid-latitude sites using **(d)** the published Kim10H calibration versus **(e)** BAYSPAR recalculated uniformly; **(f)** map of site locations. (g–h) SST at the ice-proximal Antarctic (Ross Sea shelf) sites AND-2A, CIROS-1, CRP-2, and McMurdo Erratics using **(g)** published calibrations (OPTiMAL SST and TEX^{L} subsurface temperature of Kim et al. (2012), as originally reported per site) versus **(h)** three alternative calibrations applied uniformly (Kim et al. (2010) linear calibration, Varma et al. (2024), and the MioOcean upper-ocean temperature (high-latitude Monte Carlo); **(i)** map of site locations.

https://doi.org/10.5194/essd-2026-711
Preprint. Discussion started: 2 November 2026
© Author(s) 2026. CC BY 4.0 License.

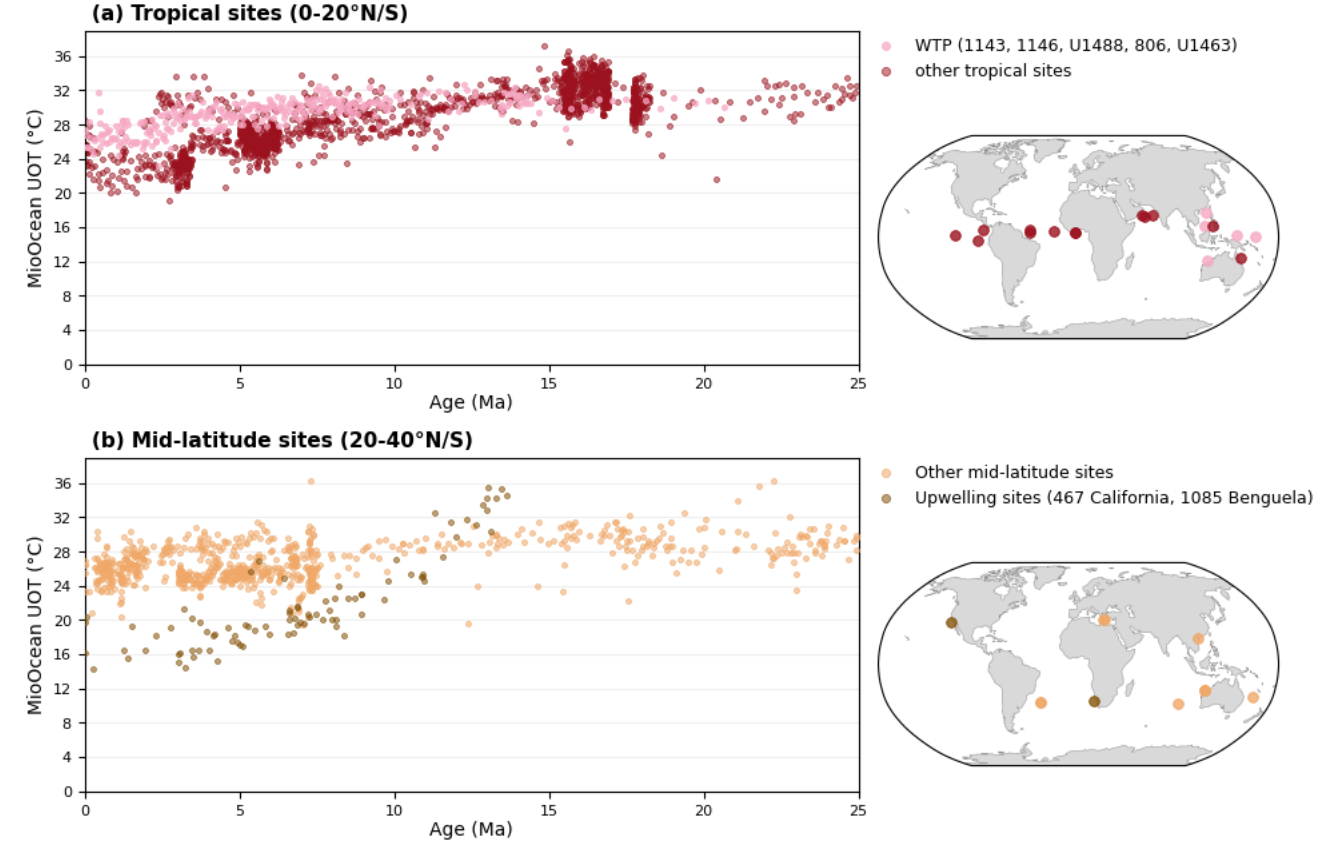


Figure B2 (a) Low latitude (0–20° N/S) stack with two distinct temperature bands. Cooler temperatures occur at sites influenced by equatorial or coastal upwelling, including the eastern equatorial Pacific (Sites 850, 846, 1241), equatorial Atlantic (Sites 925, 667, 959), and the Indian Ocean/Arabian Sea (Sites 722, 730, U1457) (dark red). In contrast, warmer conditions are consistently recorded at western tropical Pacific sites (WTP; Sites 1143, 1146, U1488, 806) (pink). **(b)** Mid-latitude stack with highlighted colder temperatures recorded at upwelling-influenced sites, including Site 467 (California Upwelling System)(dark brown triangle) and Site 1085 (Benguela Upwelling Region) (dark brown circle).

https://doi.org/10.5194/essd-2026-711
Preprint. Discussion started: 2 November 2026
© Author(s) 2026. CC BY 4.0 License.

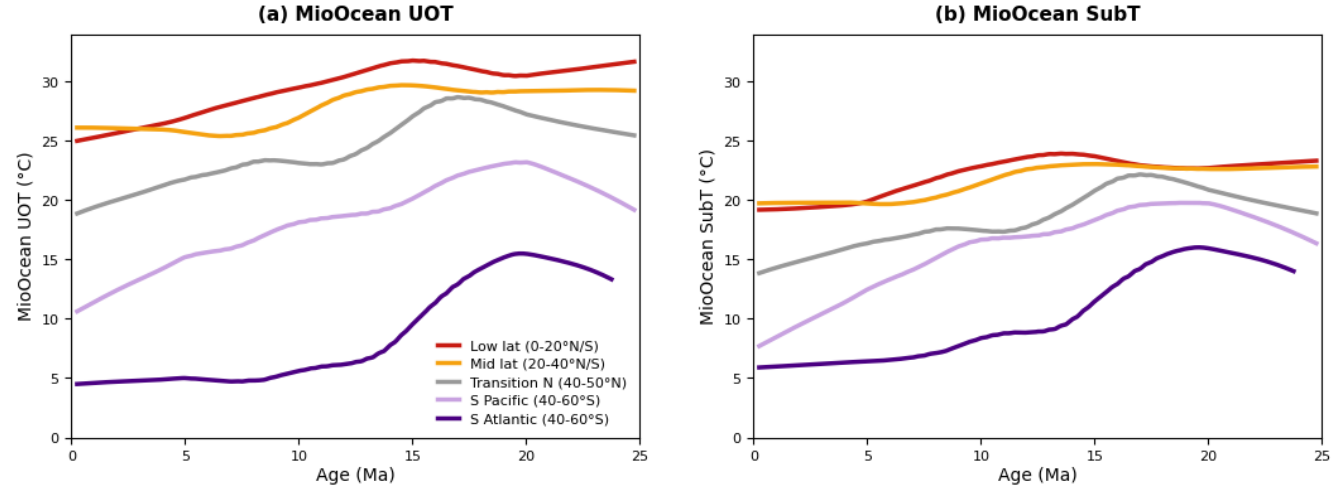


Figure B3 LOWESS-smoothed Miocene temperature trends by latitude band, comparing (a) MioOcean UOT (upper ocean temperature) and (b) MioOcean SubT. Colored lines show tricube-weighted local-linear trends fit to 0.5-Myr binned medians for five latitude bands: low latitude (0–20°N/S), mid latitude (20–40°N/S), the 40–50°N transition zone, South Pacific (40–60°S), and South Atlantic (40–60°S). The North Atlantic, North Pacific, and Antarctic bands are omitted because too few sites contribute to produce a reliable trend line. Both panels share the same y-axis scale to allow direct comparison of UOT and SubT magnitudes across latitude bands.

https://doi.org/10.5194/essd-2026-711
Preprint. Discussion started: 2 November 2026
© Author(s) 2026. CC BY 4.0 License.



Code and data availability

The MioTEX data compilation is available as part of the MioOcean database (Sosdian et al., this volume) and is openly accessible and can be downloaded directly from the MioOcean website (https://www.mioocean.com/download-data/) or through Zenodo (https://doi.org/10.5281/zenodo.22258386, Sosdian et al., 2026). This includes newly compiled datasets for TEX_{86}-derived temperatures and updated ages for TEX_{86} datasets for key sites. The Zenodo record is currently restricted; editors and reviewers have access via a private link provided to the journal. Upon acceptance, the record will be made public under the same DOI. We encourage users to also cite original data when using this data product, to provide credit to the data generators.

All code used for the MioTEX temperature compilation is publicly available on GitHub at https://github.com/audersea/mio_compilation. This includes code used for (1) calibration calculations and (2) application of screening criteria. The code for the Streamlit dashboard for MioTEX is also on GitHub at https://github.com/audersea/mio_tex. The code to generate the figures in this manuscript is at https://github.com/audersea/mio_tex_figures.

Supplement link

The link to the supplement will be included by Copernicus, if applicable.

Author contributions

AA and XL led the MioTEX working group and coordinated the compilation, quality control, validation, synthesis, and interpretation of the MioTEX dataset. AA and XL prepared the first draft of the MioTEX subsection, led its subsequent revision and developed the MioTEX code base. SF, YZ, ASh, ASl, EW, FS, and KKS contributed data, metadata, methodological expertise, validation, and review of the MioTEX subsection. SS, SM, and AH provided steering committee oversight and contributed to review and editing. All MioTEX working group members contributed to data compilation, discussion of the synthesis, and manuscript review.

Competing interests

The authors declare that they have no conflict of interest.

Disclaimer

Copernicus Publications remains neutral with regard to jurisdictional claims made in the text, published maps, institutional affiliations, or any other geographical representation in this paper. While Copernicus Publications makes every effort to include

https://doi.org/10.5194/essd-2026-711
Preprint. Discussion started: 2 November 2026
© Author(s) 2026. CC BY 4.0 License.



appropriate place names, the final responsibility lies with the authors. Views expressed in the text are those of the authors and do not necessarily reflect the views of the publisher.

Acknowledgements

We acknowledge the financial support provided by the PAGES and UKIODP to hold meetings and workshops. We also gratefully acknowledge the support of the PAGES Data Stewardship Scholarship (DSS) as part of the PlioMioVar working group, which contributed to the development of the MioOcean database, compilation pipeline, and visualization tools. We acknowledge the Miocene Temperature Data Portal (https://bolin.su.se/data/miocene-temperature-portal) as a starting point for this compilation, and the Gulf Coast, Bremen, and Kochi core repositories for IODP and related core samples and information which underpin the MioTEX work.

ASl and FS thank the Netherlands Organisation for Scientific Research Grant EMBRACER - SUMMIT.1.034., SF acknowledges funding from US NSF Grant 2303418. ASh acknowledges funding from USF NSF Grant 1947646. KKS acknowledges funding from Geocenter Denmark 2-2024. FS acknowledges funding from NWO (Dutch Research Council) grant OCENW.M.21.200. XL acknowledges funding from US NSF Grant 2436683.

Financial support

Support funds and grant agreement numbers are listed as specified upon manuscript registration and reported to FundRef upon publication.

Review statement

The review statement will be added by Copernicus Publications listing the handling editor as well as all contributing referees according to their status anonymous or identified.

https://doi.org/10.5194/essd-2026-711
Preprint. Discussion started: 2 November 2026
© Author(s) 2026. CC BY 4.0 License.



References

Auderset, A., Moretti, S., Taphorn, B., Ebner, P.-R., Kast, E., Wang, X. T., Schiebel, R., Sigman, D. M., Haug, G. H., and Martínez-García, A.: Enhanced ocean oxygenation during Cenozoic warm periods, Nature, 609, 77–82, https://doi.org/10.1038/s41586-022-05017-0, 2022.

Besiou, E., Vasiliev, I., Kontakiotis, G., Agiadi, K., Methner, K., Mulch, A., Krijgsman, W., and Antonarakou, A.: Large and rapid salinity fluctuations affected the eastern Mediterranean at the Tortonian–Messinian transition, Palaeogeography, Palaeoclimatology, Palaeoecology, 656, 112568, 2024.

Bijl, P. K., Śliwińska, K. K., Duncan, B., Huguet, A., Naeher, S., Rattanasriampaipong, R., Sosa-Montes de Oca, C., Auderset, A., Berke, M. A., Kim, B. S., Davtian, N., Dunkley Jones, T., Eefting, D. D., Elling, F. J., Fenies, P., Inglis, G. N., O'Connor, L., Pancost, R. D., Peterse, F., Rice, A., Sluijs, A., Varma, D., Xiao, W., and Zhang, Y. G.: Reviews and syntheses: Best practices for the application of marine GDGTs as proxy for paleotemperatures: sampling, processing, analyses, interpretation, and archiving protocols, Biogeosciences, 22, 6465–6508, 10.5194/bg-22-6465-2025, 2025.

Blaga, C. I., Reichart, G.-J., Heiri, O., and Damsté, J. S. S.: Tetraether membrane lipid distributions in water-column particulate matter and sediments: a study of 47 European lakes along a north–south transect, Journal of Paleolimnology, 41, 523–540, 2009.

Browne, I. M., Shevenell, A., Leckie, R. M., Dodd, J. P., Christopoulou, M.-E., Sangiorgi, F., Wubben, E., Prebble, J., Ash, J., van Peer, T. E., Harwood, D. M., Levy, R. H., Mckay, R. M., De Santis, L., and Kulhanek, D. K.: Antarctic Ice Sheet growth during the Miocene Climatic Optimum, AGU Fall Meeting Abstracts, Chicago, IL, December 01, 20222022.

Burls, N. J., Bradshaw, C., De Boer, A. M., Herold, N., Huber, M., Pound, M., Donnadieu, Y., Farnsworth, A., Frigola, A., and Gasson, E.: Simulating Miocene warmth: insights from an opportunistic Multi-Model ensemble (MioMIP1), Paleoceanography and Paleoclimatology, 36, e2020PA004054, /10.1029/2020PA004054, 2021.

Burls, N. J., Wright, N. M., Acosta, R. P., Bradshaw, C. D., Gasson, E., Stap, L. B., Ramstein, G., Halberstadt, A. R. W., De Boer, A. M., Akgün, F., Cantrill, D. J., Casas-Gallego, M., Doláková, N., Erdei, B., Farnsworth, A., Feakins, S., Feng, R., Fletcher, T., Fluteau, F., Green, J. A. M., von der Heydt, A. S., Huber, M., Hutchinson, D. K., Ivanov, D., Kayseri-Özer, M. S., Knorr, G., Kováčová, M., Lear, C. H., LeGrande, A. N., Li, S., Liu, X., Lunt, D. J., Meissner, K., Miao, Y., Naik, T. J., Navarro, J. B., Novak, J. B., Ochoa, D., Paxman, G. J. G., Pound, M. J., Rae, J. W. B., Reichgelt, T., Renoult, M., Sangiorgi, F., Sarr, A. C., Segalla, D., Sepulchre, P., Shevenell, A., Steinig, S., Straume, E., Strömberg, C. A. E., Tabor, C., Utescher, T., Weiffenbach, J. E., Worobiec, E., Zhang, Y., Zhu, F., Zhu, J., Auderset, A., Colleoni, F., Dolan, A., Havranek, R., Holbourn, A., Herold, N., Lee, D., Marschalek, J. W., Mitsunaga, B., Modestou, S., Perez-Angel, L., Saslaw, M., Sosdian, S., Stiles, E., Sun, Y., Tan, N., Zhang, Z., and Zhao, Y.: MioMIP2: Experimental design for Phase 1 & 2 of the Miocene component of the CMIP7/PMIP7 Deep-time Model Intercomparison Project (DeepMIP-Miocene), EGUsphere, 2026, 1–88, 10.5194/egusphere-2026-3595, 2026.

Christensen, B. A., Renema, W., Henderiks, J., De Vleeschouwer, D., Groeneveld, J., Castañeda, I. S., Reuning, L., Bogus, K., Auer, G., and Ishiwa, T.: Indonesian Throughflow drove Australian climate from humid Pliocene to arid Pleistocene, Geophysical Research Letters, 44, 6914–6925, 2017.

Church, M. J., DeLong, E. F., Ducklow, H. W., Karner, M. B., Preston, C. M., and Karl, D. M.: Abundance and distribution of planktonic Archaea and Bacteria in the waters west of the Antarctic Peninsula, Limnology and Oceanography, 48, 1893–1902, 2003.

Cramer, B., Miller, K., Barrett, P., and Wright, J.: Late Cretaceous–Neogene trends in deep ocean temperature and continental ice volume: Reconciling records of benthic foraminiferal geochemistry (δ18O and Mg/Ca) with sea level history, Journal of Geophysical Research: Oceans, 116, 2011.

Here's the same ESSD format. Note that this one is still at "File validation" stage — it hasn't been assigned a preprint number or DOI yet, so I've left a placeholder where the DOI will go:

Drury, A. J., Tangunan, D. N., Liebrand, D., Auer, G., Kasbohm, J., King, D. J., Westerhold, T., Crocker, A. J., Kochhann, K. G. D., Kuhnt, W., Ochoa, D., van Peer, T. E., Krijgsman, W., Robinson, M. M., Shah, N. S., Sibert, E. C., Wade, B. S., Sosdian, S. M., Auderset, A., Modestou, S., and Holbourn, A.: The MioOcean Age Framework: an age model database and chronoinformatics approach for synchronised Miocene ocean temperature, climate and proxy records, Earth Syst. Sci. Data Discuss. [preprint], 2026

https://doi.org/10.5194/essd-2026-711
Preprint. Discussion started: 2 November 2026
© Author(s) 2026. CC BY 4.0 License.

Duncan, B., McKay, R. M., Levy, R. H., Naish, T. R., Prebble, J. G., Sangiorgi, F., Krishnan, S., Hoem, F., Clowes, C., Dunkley Jones, T., Gasson, E. G. W., Kraus, C., Kulhanek, D. K., Meyers, S. R., Moossen, H., Warren, C. E., Willmott, V., Ventura, G. T., and Bendle, J. A.: GDGT abundances and indices for Ross Sea sample sites, PANGAEA [dataset], 10.1594/PANGAEA.946782, 2022.

Dunkley Jones, T., Eley, Y. L., Thomson, W., Greene, S. E., Mandel, I., Edgar, K., and Bendle, J. A.: OPTiMAL: a new machine learning approach for GDGT-based palaeothermometry, Climate of the Past, 16, 2599–2617, 2020.

Elling, F. J., Inglis, G. N., Davtian, N., Hurley, S. J., Naafs, B. D. A., O'Connor, L. K., Pancost, R. D., Peterse, F., Rattanasriampaipong, R., and Rice, A.: Archaeal tetraether lipids as tracers for past marine environmental change, Paleoceanography and Paleoclimatology, 41, e2025PA005373, 2026.

Evangelinos, D., Escutia, C., Etourneau, J., Hoem, F., Bijl, P., Boterblom, W., van de Flierdt, T., Valero, L., Flores, J.-A., and Rodriguez-Tovar, F. J.: Late oligocene-miocene proto-antarctic circumpolar current dynamics off the Wilkes Land margin, East Antarctica, Global and Planetary Change, 191, 103221, /10.1016/j.gloplacha.2020.103221, 2020.

Feakins, S. J., Liddy, H. M., Tauxe, L., Galy, V., Feng, X., Tierney, J. E., Miao, Y., and Warny, S.: Miocene C4 grassland expansion as recorded by the Indus Fan, Paleoceanography and Paleoclimatology, 35, e2020PA003856, /10.1029/2020PA003856, 2020.

Flower, B. P. and Kennett, J. P.: The middle Miocene climatic transition: East Antarctic ice sheet development, deep ocean circulation and global carbon cycling, Palaeogeography, palaeoclimatology, palaeoecology, 108, 537–555, 1994.

Fokkema, C. D., Agterhuis, T., Gerritsma, D., de Goeij, M., Liu, X., de Regt, P., Rice, A., Vennema, L., Agnini, C., Bijl, P. K., Frieling, J., Huber, M., Peterse, F., and Sluijs, A.: Polar amplification of orbital-scale climate variability in the early Eocene greenhouse world, Clim. Past, 20, 1303–1325, 10.5194/cp-20-1303-2024, 2024.

Gasson, E., DeConto, R. M., Pollard, D., and Levy, R. H.: Dynamic Antarctic ice sheet during the early to mid-Miocene, Proceedings of the National Academy of Sciences, 113, 3459–3464, 2016.

Guitián, J., Phelps, S., Polissar, P. J., Ausín, B., Eglinton, T. I., and Stoll, H. M.: Midlatitude Temperature Variations in the Oligocene to Early Miocene, Paleoceanography and Paleoclimatology, 34, 1328–1343, /10.1029/2019PA003638, 2019.

Hartman, J. D., Sangiorgi, F., Salabarnada, A., Peterse, F., Houben, A. J., Schouten, S., Brinkhuis, H., Escutia, C., and Bijl, P. K.: Paleoceanography and ice sheet variability offshore Wilkes Land, Antarctica–Part 3: Insights from Oligocene–Miocene TEX 86-based sea surface temperature reconstructions, Climate of the Past, 14, 1275–1297, 2018.

He, Y., Wang, H., and Liu, Z.: Development of the Leeuwin Current on the northwest shelf of Australia through the Pliocene-Pleistocene period, Earth Planet Sc Lett, 559, 116767, /10.1016/j.epsl.2021.116767, 2021.

Herbert, T. D., Dalton, C. A., Liu, Z., Salazar, A., Si, W., and Wilson, D. S.: Tectonic degassing drove global temperature trends since 20 Ma, Science, 377, 116–119, /10.1126/science.abl4353, 2022.

Herbert, T. D., Lawrence, K. T., Tzanova, A., Peterson, L. C., Caballero-Gill, R., and Kelly, C. S.: Late Miocene global cooling and the rise of modern ecosystems, Nat Geosci, 9, 843–847, /10.1038/ngeo2813, 2016.

Hernández-Sánchez, M., Woodward, E., Taylor, K., Henderson, G., and Pancost, R.: Variations in GDGT distributions through the water column in the South East Atlantic Ocean, Geochim Cosmochim Ac, 132, 337–348, 2014.

Ho, S. L. and Laepple, T.: Flat meridional temperature gradient in the early Eocene in the subsurface rather than surface ocean, Nat Geosci, 9, 606–610, 2016.

Hoem, F. S., Sauermilch, I., Aleksinski, A. K., Huber, M., Peterse, F., Sangiorgi, F., and Bijl, P. K.: Strength and variability of the Oligocene Southern Ocean surface temperature gradient, Communications Earth & Environment, 3, 322, /10.1038/s43247-022-00666-5, 2022.

Hopmans, E. C., Weijers, J. W., Schefuß, E., Herfort, L., Damsté, J. S. S., and Schouten, S.: A novel proxy for terrestrial organic matter in sediments based on branched and isoprenoid tetraether lipids, Earth Planet Sc Lett, 224, 107–116, https://doi.org/10.1016/j.epsl.2004.05.012, 2004.

Hou, S., Lamprou, F., Hoem, F. S., Hadju, M. R. N., Sangiorgi, F., Peterse, F., and Bijl, P. K.: Lipid biomarker-based sea (sub) surface temperature record offshore Tasmania over the last 23 million years, Climate of the Past Discussions, 2022, 1–33, /10.5194/cp-19-787-2023, 2022.

Hou, S., Stap, L. B., Paul, R., Nelissen, M., Hoem, F. S., Ziegler, M., Sluijs, A., Sangiorgi, F., and Bijl, P. K.: Reconciling Southern Ocean fronts equatorward migration with minor Antarctic ice volume change during Miocene cooling, Nature Communications, 14, 7230, 10.1038/s41467-023-43106-4, 2023.

https://doi.org/10.5194/essd-2026-711
Preprint. Discussion started: 2 November 2026
© Author(s) 2026. CC BY 4.0 License.

Hurley, S. J., Lipp, J. S., Close, H. G., Hinrichs, K.-U., and Pearson, A.: Distribution and export of isoprenoid tetraether lipids in suspended particulate matter from the water column of the Western Atlantic Ocean, Organic geochemistry, 116, 90–102, 2018.

Inglis, G. N., Farnsworth, A., Lunt, D., Foster, G. L., Hollis, C. J., Pagani, M., Jardine, P. E., Pearson, P. N., Markwick, P., Galsworthy, A. M. J., Raynham, L., Taylor, K. W. R., and Pancost, R. D.: Descent toward the Icehouse: Eocene sea surface cooling inferred from GDGT distributions, Paleoceanography, 2015.

Kim, J.-H., Schouten, S., Hopmans, E. C., Donner, B., and Damsté, J. S. S.: Global sediment core-top calibration of the TEX86 paleothermometer in the ocean, Geochim Cosmochim Ac, 72, 1154–1173, 2008.

Kim, J.-H., Van der Meer, J., Schouten, S., Helmke, P., Willmott, V., Sangiorgi, F., Koç, N., Hopmans, E. C., and Damsté, J. S. S.: New indices and calibrations derived from the distribution of crenarchaeal isoprenoid tetraether lipids: Implications for past sea surface temperature reconstructions, Geochim Cosmochim Ac, 74, 4639–4654, https://doi.org/10.1016/j.gca.2010.05.027, 2010.

Kim, J. H., Crosta, X., Willmott, V., Renssen, H., Bonnin, J., Helmke, P., Schouten, S., and Sinninghe Damsté, J. S.: Holocene subsurface temperature variability in the eastern Antarctic continental margin, Geophysical Research Letters, 39, 2012.

Kontakiotis, G., Butiseacă, G. A., Antonarakou, A., Agiadi, K., Zarkogiannis, S. D., Krsnik, E., Besiou, E., Zachariasse, W. J., Lourens, L., and Thivaiou, D.: Hypersalinity accompanies tectonic restriction in the eastern Mediterranean prior to the Messinian Salinity Crisis, Palaeogeography, Palaeoclimatology, Palaeoecology, 592, 110903, 2022.

Lagabrielle, Y., Goddéris, Y., Donnadieu, Y., Malavieille, J., and Suarez, M.: The tectonic history of Drake Passage and its possible impacts on global climate, Earth Planet Sc Lett, 279, 197–211, https://doi.org/10.1016/j.epsl.2008.12.037, 2009.

Lawrence, K., Pearson, A., Castañeda, I., Ladlow, C., Peterson, L., and Lawrence, C.: Comparison of late Neogene Uk′ 37 and TEX86 paleotemperature records from the eastern equatorial Pacific at orbital resolution, Paleoceanography and Paleoclimatology, 35, e2020PA003858, https://doi.org/10.1029/2020PA003858, 2020.

Leutert, T. J., Auderset, A., Martínez-García, A., Modestou, S., and Meckler, A. N.: Coupled Southern Ocean cooling and Antarctic ice sheet expansion during the middle Miocene, Nat Geosci, 13, 634–639, https://doi.org/10.1038/s41561-020-0623-0, 2020.

Levy, R., Harwood, D., Florindo, F., Sangiorgi, F., Tripati, R., Von Eynatten, H., Gasson, E., Kuhn, G., Tripati, A., and DeConto, R.: Antarctic ice sheet sensitivity to atmospheric CO2 variations in the early to mid-Miocene, Proceedings of the National Academy of Sciences, 113, 3453–3458, /10.1073/pnas.1516030113, 2016.

Li, Z., Zhang, Y. G., Torres, M., and Mills, B. J.: Neogene burial of organic carbon in the global ocean, Nature, 613, 90–95, /10.1038/s41586-022-05413-6, 2023.

Liebrand, D., De Bakker, A. T., Beddow, H. M., Wilson, P. A., Bohaty, S. M., Ruessink, G., Pälike, H., Batenburg, S. J., Hilgen, F. J., and Hodell, D. A.: Evolution of the early Antarctic ice ages, Proceedings of the National Academy of Sciences, 114, 3867–3872, 2017.

Liu, X., Huber, M., Foster, G. L., Dessler, A., and Zhang, Y. G.: Persistent high latitude amplification of the Pacific Ocean over the past 10 million years, Nature Communications, 13, 7310, /10.1038/s41467-022-35011-z, 2022.

Liu, Z., Pagani, M., Zinniker, D., DeConto, R., Huber, M., Brinkhuis, H., Shah, S. R., Leckie, R. M., and Pearson, A.: Global cooling during the Eocene-Oligocene climate transition, Science, 323, 1187–1190, https://doi.org/10.1126/science.1166368, 2009.

Mather, B. R., Müller, R. D., Zahirovic, S., Cannon, J., Chin, M., Ilano, L., Wright, N. M., Alfonso, C., Williams, S., and Tetley, M.: Deep time spatio-temporal data analysis using py GP lates with P late T ectonic T ools and GP lately, Geoscience Data Journal, /10.1002/gdj3.185, 2023.

Merdith, A. S., Williams, S. E., Collins, A. S., Tetley, M. G., Mulder, J. A., Blades, M. L., Young, A., Armistead, S. E., Cannon, J., and Zahirovic, S.: Extending full-plate tectonic models into deep time: Linking the Neoproterozoic and the Phanerozoic, Earth-science reviews, 214, 103477, 2021.

Miller, K. G., Browning, J. V., Schmelz, W. J., Kopp, R. E., Mountain, G. S., and Wright, J. D.: Cenozoic sea-level and cryospheric evolution from deep-sea geochemical and continental margin records, Science advances, 6, eaaz1346, https://doi.org/10.1126/sciadv.aaz1346, 2020.

Mulvaney, R., Abram, N. J., Hindmarsh, R. C., Arrowsmith, C., Fleet, L., Triest, J., Sime, L. C., Alemany, O., and Foord, S.: Recent Antarctic Peninsula warming relative to Holocene climate and ice-shelf history, Nature, 489, 141–144, 2012.

https://doi.org/10.5194/essd-2026-711
Preprint. Discussion started: 2 November 2026
© Author(s) 2026. CC BY 4.0 License.



Murray, A., Preston, C., Massana, R., Taylor, L. T., Blakis, A., Wu, K., and DeLong, E. F.: Seasonal and spatial variability of bacterial and archaeal assemblages in the coastal waters near Anvers Island, Antarctica, Applied and Environmental Microbiology, 64, 2585–2595, 1998.

O'Brien, C. L., Robinson, S. A., Pancost, R. D., Sinninghe Damsté, J. S., Schouten, S., Lunt, D. J., Alsenz, H., Bornemann, A., Bottini, C., Brassell, S. C., Farnsworth, A., Forster, A., Huber, B. T., Inglis, G. N., Jenkyns, H. C., Linnert, C., Littler, K., Markwick, P., McAnena, A., Mutterlose, J., Naafs, B. D. A., Püttmann, W., Sluijs, A., van Helmond, N. A. G. M., Vellekoop, J., Wagner, T., and Wrobel, N. E.: Cretaceous sea-surface temperature evolution: Constraints from TEX86 and planktonic foraminiferal oxygen isotopes, Earth-Science Reviews, 172, 224–247, https://doi.org/10.1016/j.earscirev.2017.07.012, 2017.

O'Brien, C. L., Huber, M., Thomas, E., Pagani, M., Super, J. R., Elder, L. E., and Hull, P. M.: The enigma of Oligocene climate and global surface temperature evolution, Proceedings of the National Academy of Sciences, 117, 25302–25309, https://doi.org/10.1073/pnas.2003914117, 2020.

O'Dea, A., Lessios, H. A., Coates, A. G., Eytan, R. I., Restrepo-Moreno, S. A., Cione, A. L., Collins, L. S., De Queiroz, A., Farris, D. W., and Norris, R. D.: Formation of the Isthmus of Panama, Science advances, 2, e1600883, https://doi.org/10.1126/sciadv.1600883, 2016.

Pearson, A. and Ingalls, A. E.: Assessing the use of archaeal lipids as marine environmental proxies, Annual Review of Earth and Planetary Sciences, 41, 359–384, 2013.

Peterse, F., Kim, J.-H., Schouten, S., Kristensen, D. K., Koç, N., and Damsté, J. S. S.: Constraints on the application of the MBT/CBT palaeothermometer at high latitude environments (Svalbard, Norway), Organic Geochemistry, 40, 692–699, 2009.

Petrick, B., Reuning, L., Auer, G., Zhang, Y., Pfeiffer, M., and Schwark, L.: Warm, not cold temperatures contributed to a Late Miocene reef decline in the Coral Sea, Scientific Reports, 13, 4015, /10.1038/s41598-023-31034-8, 2023.

Pound, M. J., Haywood, A. M., Salzmann, U., and Riding, J. B.: Global vegetation dynamics and latitudinal temperature gradients during the Mid to Late Miocene (15.97–5.33 Ma), Earth-Science Reviews, 112, 1–22, 2012.

Rattanasriampaipong, R., Tierney, J. E., and Inglis, G. N.: TEXAS: A proxy system model for TEX86 paleothermometry, ESS Open Archive, 2026.

Rattanasriampaipong, R., Tierney, J. E., Abell, J. T., and Gilmore, L. D.: A nutrient effect on the TEX86 paleotemperature proxy, Geophysical Research Letters, 52, e2025GL115237, 2025.

Rattanasriampaipong, R., Zhang, Y. G., Pearson, A., Hedlund, B. P., and Zhang, S.: Archaeal lipids trace ecology and evolution of marine ammonia-oxidizing archaea, Proceedings of the National Academy of Sciences, 119, e2123193119, doi:10.1073/pnas.2123193119, 2022.

Rommerskirchen, F., Condon, T., Mollenhauer, G., Dupont, L., and Schefuss, E.: Miocene to Pliocene development of surface and subsurface temperatures in the Benguela Current system, Paleoceanography, 26, https://doi.org/10.1029/2010PA002074, 2011.

Sabino, M., Pierre, F. D., Natalicchio, M., Birgel, D., Gier, S., and Peckmann, J.: The response of water column and sedimentary environments to the advent of the Messinian salinity crisis: insights from an onshore deep-water section (Govone, NW Italy), Geological Magazine, 158, 825–841, /10.1017/S0016756820000874, 2021.

Salocchi, A. C., Krawielicki, J., Eglinton, T. I., Fioroni, C., Fontana, D., Conti, S., and Picotti, V.: Biomarker constraints on Mediterranean climate and ecosystem transitions during the Early-Middle Miocene, Palaeogeography, Palaeoclimatology, Palaeoecology, 562, 110092, 2021.

Sangiorgi, F., Quaijtaal, W., Donders, T. H., Schouten, S., and Louwye, S.: Middle Miocene temperature and productivity evolution at a Northeast Atlantic shelf site (IODP U1318, Porcupine Basin): Global and regional changes, Paleoceanography and Paleoclimatology, 36, e2020PA004059, /10.1029/2020PA004059, 2021.

Sangiorgi, F., Bijl, P. K., Passchier, S., Salzmann, U., Schouten, S., McKay, R., Cody, R. D., Pross, J., Van De Flierdt, T., and Bohaty, S. M.: Southern Ocean warming and Wilkes Land ice sheet retreat during the mid-Miocene, Nature communications, 9, 1–11, /10.1038/s41467-017-02609-7, 2018.

Schouten, S., Hopmans, E. C., Schefuß, E., and Damste, J. S. S.: Distributional variations in marine crenarchaeotal membrane lipids: a new tool for reconstructing ancient sea water temperatures?, Earth Planet Sc Lett, 204, 265–274, https://doi.org/10.1016/S0012-821X(02)00979-2, 2002.

https://doi.org/10.5194/essd-2026-711
Preprint. Discussion started: 2 November 2026
© Author(s) 2026. CC BY 4.0 License.



Seki, O., Schmidt, D. N., Schouten, S., Hopmans, E. C., Sinninghe Damsté, J. S., and Pancost, R. D.: Paleoceanographic changes in the Eastern Equatorial Pacific over the last 10 Myr, Paleoceanography, 27, 2012.

Shevenell, A. E., Kennett, J. P., and Lea, D. W.: Middle Miocene southern ocean cooling and Antarctic cryosphere expansion, Science, 305, 1766–1770, /10.1126/science.1100061, 2004.

Shevenell, A. E., Kennett, J. P., and Lea, D. W.: Middle Miocene ice sheet dynamics, deep-sea temperatures, and carbon cycling: A Southern Ocean perspective, Geochemistry, Geophysics, Geosystems, 9, 2008.

Shevenell, A. E., Ingalls, A., Domack, E., and Kelly, C.: Holocene Southern Ocean surface temperature variability west of the Antarctic Peninsula, Nature, 470, 250–254, 2011.

Sinninghe Damsté, J. S.: Spatial heterogeneity of sources of branched tetraethers in shelf systems: The geochemistry of tetraethers in the Berau River delta (Kalimantan, Indonesia), Geochim Cosmochim Ac, 186, 13–31, https://doi.org/10.1016/j.gca.2016.04.033, 2016.

Sinninghe Damsté, J. S., Ossebaar, J., Schouten, S., and Verschuren, D.: Distribution of tetraether lipids in the 25-ka sedimentary record of Lake Challa: extracting reliable TEX86 and MBT/CBT palaeotemperatures from an equatorial African lake, Quaternary Science Reviews, 50, 43–54, /10.1016/j.quascirev.2012.07.001, 2012.

Sinninghe Damsté, J. S., Schouten, S., Hopmans, E. C., van Duin, A. C., and Geenevasen, J. A.: Crenarchaeol the characteristic core glycerol dibiphytanyl glycerol tetraether membrane lipid of cosmopolitan pelagic crenarchaeota, Journal of lipid research, 43, 1641–1651, 2002.

Sosdian, S. M., Auderset, A., Modestou, S., Holbourn, A., Boscolo-Galazzo, F., Drury, A. J., Hess, A. V., Kochhann, K. G. D., Liebrand, D., Liu, X., Nirenberg, J., Shah, N. S., Tangunan, D., Auer, G., Badger, M. P. S., Bolton, C., Clark, A., Crocker, A., Evans, D., Feakins, S., Herbert, T., Judd, E., Kasbohm, J., King, D., Krijgsman, W., Kuhnt, W., Lawrence, K., Lear, C. H., Marshall-Mills, K., McClymont, E., Meckler, N., Minton, P., Nilsson-Kerr, K., Ochoa, D., Robinson, M., Sakthivel, T., Sangiorgi, F., Shevenell, A. E., Si, W., Sibert, E., Sliwinska, K. K., Sluijs, A., Stoll, H., Taylor, V., van Peer, T., Wade, B., Westerhold, T., Wubben, E., Zhang, Y., and Ziegler, M.: MioOcean: database compilation and temperature proxy systematics in the Miocene oceans, Earth Syst. Sci. Data Discuss. [preprint], 2026

Sosdian, S., Auderset, A., Modestou, S., Holbourn, A., and the MioOcean Working Group: *MioOcean temperature compilation,* Zenodo [data set],https://doi.org/10.5281/zenodo.22258386, 2026.

Steinthorsdottir, M., Coxall, H., De Boer, A., Huber, M., Barbolini, N., Bradshaw, C., Burls, N., Feakins, S., Gasson, E., and Henderiks, J.: The Miocene: the future of the past, Paleoceanography and Paleoclimatology, 36, e2020PA004037, 2021.

Super, J. R., Thomas, E., Pagani, M., Huber, M., O'Brien, C., and Hull, P. M.: North Atlantic temperature and pCO2 coupling in the early-middle Miocene, Geology, 46, 519–522, /10.1130/G40228.1, 2018.

Super, J. R., Thomas, E., Pagani, M., Huber, M., O'Brien, C. L., and Hull, P. M.: Miocene evolution of North Atlantic sea surface temperature, Paleoceanography and Paleoclimatology, 35, e2019PA003748, /10.1029/2019PA003748, 2020.

Taylor, K. W., Huber, M., Hollis, C. J., Hernandez-Sanchez, M. T., and Pancost, R. D.: Re-evaluating modern and Palaeogene GDGT distributions: Implications for SST reconstructions, Global and Planetary Change, 108, 158–174, 2013.

Tierney, J. E. and Tingley, M. P.: A Bayesian, spatially-varying calibration model for the TEX86 proxy, Geochim Cosmochim Ac, 127, 83–106, https://doi.org/10.1016/j.gca.2013.11.026, 2014.

Tolar, B. B., Powers, L. C., Miller, W. L., Wallsgrove, N. J., Popp, B. N., and Hollibaugh, J. T.: Ammonia oxidation in the ocean can be inhibited by nanomolar concentrations of hydrogen peroxide, Frontiers in Marine Science, 3, 237, 2016.

Tsopouridis, L., Spengler, T., and Spensberger, C.: Smoother versus sharper Gulf Stream and Kuroshio sea surface temperature fronts: Effects on cyclones and climatology, Weather and Climate Dynamics, 2, 953–970, 2021.

Vadman, K. J.: Past Ice-Ocean Interactions on the Sabrina Coast shelf, East Antarctica: Deglacial to Recent Paleoenvironmental Insights from Marine Sediments, 2021.

Van Der Weijst, C. M., Van Der Laan, K. J., Peterse, F., Reichart, G.-J., Sangiorgi, F., Schouten, S., Veenstra, T. J., and Sluijs, A.: A 15-million-year surface-and subsurface-integrated TEX86 temperature record from the eastern equatorial Atlantic, Climate of the Past, 18, 1947–1962, /10.5194/cp-18-1947-2022, 2022.

Varma, D., Hopmans, E. C., Van Kemenade, Z. R., Kusch, S., Berg, S., Bale, N. J., Sangiorgi, F., Reichart, G.-J., Damsté, J. S. S., and Schouten, S.: Evaluating isoprenoidal hydroxylated GDGT-based temperature proxies in surface sediments from the global ocean, Geochim Cosmochim Ac, 370, 113–127, 2024.

https://doi.org/10.5194/essd-2026-711
Preprint. Discussion started: 2 November 2026
© Author(s) 2026. CC BY 4.0 License.

Wang, H., Liu, W., Lu, H., Zhang, Y., Liang, Y., He, Y., Bohaty, S. M., Wilson, P. A., and Liu, Z.: Oxygenated deep waters fed early Atlantic overturning circulation upon Antarctic glaciation, Nat Geosci, 16, 1014–1019, 10.1038/s41561-023-01292-2, 2023.

Wang, M., Wang, H., Zhu, Z., Yang, X., Zhang, K., Zhang, Y., Liu, W., Zheng, Z., Zong, Y., and Liu, Z.: Late Miocene-Pliocene Asian summer monsoon variability linked to both tropical Pacific temperature and Walker Circulation, Earth Planet Sc Lett, 561, 116823, 2021.

Warny, S., Askin, R. A., Hannah, M. J., Mohr, B. A., Raine, J. I., Harwood, D. M., Florindo, F., and Team, S. S.: Palynomorphs from a sediment core reveal a sudden remarkably warm Antarctica during the middle Miocene, Geology, 37, 955–958, 2009.

Weijers, J. W., Lim, K. L., Aquilina, A., Sinninghe Damsté, J. S., and Pancost, R. D.: Biogeochemical controls on glycerol dialkyl glycerol tetraether lipid distributions in sediments characterized by diffusive methane flux, Geochemistry, Geophysics, Geosystems, 12, /10.1029/2011GC003724, 2011.

Weijers, J. W. H., Schouten, S., Spaargaren, O. C., and Sinninghe Damsté, J. S.: Occurrence and distribution of tetraether membrane lipids in soils: Implications for the use of the TEX86 proxy and the BIT index, Organic Geochemistry, 37, 1680–1693, https://doi.org/10.1016/j.orggeochem.2006.07.018, 2006.

Witkowski, C. R., von der Heydt, A. S., Valdes, P. J., van der Meer, M. T. J., Schouten, S., and Sinninghe Damsté, J. S.: Continuous sterane and phytane $\delta^{13}C$ record reveals a substantial pCO_2 decline since the mid-Miocene, Nature Communications, 2024.

Wubben, E., Liu, X., Veenstra, T. J. T., Acosta, R. P., den Hollander, J., Overduin, C., Huber, M., Sangiorgi, F., Peterse, F., and Sluijs, A.: Ocean circulation changes rather than global warming drove temperature trends across the Miocene Climatic Optimum, Science Advances, 2026.

Wubben, E., Spiering, B. R., Veenstra, T., Bos, R., Wang, Z., van Dijk, J., Raffi, I., Witkowski, J., Hilgen, F. J., and Peterse, F.: Tropical warming and intensification of the West African monsoon during the Miocene climatic Optimum, Paleoceanography and Paleoclimatology, 39, e2023PA004767, 2024.

Xiao, W., Wang, Y., Zhou, S., Hu, L., Yang, H., and Xu, Y.: Ubiquitous production of branched glycerol dialkyl glycerol tetraethers (brGDGTs) in global marine environments: a new source indicator for brGDGTs, Biogeosciences, 13, 5883–5894, https://doi.org/10.5194/bg-13-5883-2016, 2016.

Yamamoto, M. and Kobayashi, D.: Surface ocean cooling in the subarctic North Pacific during the late Pliocene suggests an atmospheric reorganization prior to extensive Northern Hemisphere glaciation, Deep Sea Research Part II: Topical Studies in Oceanography, 125, 177–183, /10.1016/j.dsr2.2015.03.005, 2016.

Zahirovic, S., Eleish, A., Doss, S., Pall, J., Cannon, J., Pistone, M., Tetley, M. G., Young, A., and Fox, P.: Subduction and carbonate platform interactions, Geoscience Data Journal, 9, 371–383, 2022.

Zhang, Y. G. and Liu, X.: Export depth of the TEX86 signal, Paleoceanography and Paleoclimatology, 33, 666–671, 2018.

Zhang, Y. G., Pagani, M., and Liu, Z.: A 12-million-year temperature history of the tropical Pacific Ocean, Science, 344, 84–87, /10.1126/science.1246172, 2014.

Zhang, Y. G., Pagani, M., and Wang, Z.: Ring Index: A new strategy to evaluate the integrity of TEX86 paleothermometry, Paleoceanography, 31, 220–232, /10.1002/2015PA002848, 2016.

Zhang, Y. G., Pagani, M., Liu, Z. H., Bohaty, S. M., and DeConto, R.: A 40-million-year history of atmospheric CO2, Philos T R Soc A, 371, /10.1098/rsta.2013.0096, 2013.

Zhang, Y. G., Zhang, C. L., Liu, X.-L., Li, L., Hinrichs, K.-U., and Noakes, J. E.: Methane Index: A tetraether archaeal lipid biomarker indicator for detecting the instability of marine gas hydrates, Earth Planet Sc Lett, 307, 525–534, /10.1016/j.epsl.2011.05.031, 2011.

Zhuang, G., Pagani, M., and Zhang, Y. G.: Monsoonal upwelling in the western Arabian Sea since the middle Miocene, Geology, 45, 655–658, /10.1130/G39013.1, 2017.